Article

Immunity

Innate type 2 immunity controls hair follicle commensalism by *Demodex* mites

Graphical abstract

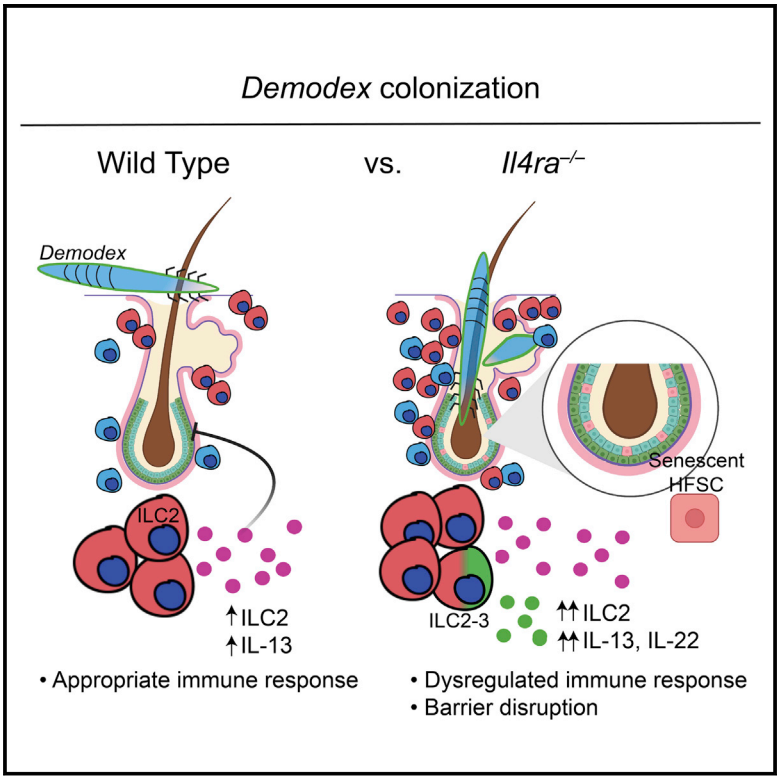

Highlights

- Type 2 innate immunity is critical for normal commensalism with *Demodex*
- In the absence of type 2 immunity, *Demodex* causes aberrant inflammation
- IL-13 from ILC2s is coupled to the hair cycle and restrains stem cell proliferation
- Decreased type 2 cytokine expression is observed in patients with rhinophyma

Authors

Roberto R. Ricardo-Gonzalez, Maya E. Kotas, Claire E. O'Leary, ..., Matthew H. Spitzer, Hong-Erh Liang, Richard M. Locksley

Correspondence

roberto.ricardo-gonzalez@ucsf.edu (R.R.R.-G.), richard.locksley@ucsf.edu (R.M.L.)

In brief

Type 2 cytokines are well recognized for their role in mediating allergic pathologies in skin, but their role in normal skin physiology is unclear. Ricardo-Gonzalez et al. reveal that type 2 immunity restrains skin inflammation in response to injury that is necessary to control hair follicle commensalism by *Demodex* mites.

Ricardo-Gonzalez et al., 2022, Immunity *55*, 1891–1908
October 11, 2022
https://doi.org/10.1016/j.immuni.2022.08.001

CellPress

Immunity

CellPress
OPEN ACCESS

Article

Innate type 2 immunity controls hair follicle commensalism by *Demodex* mites

Roberto R. Ricardo-Gonzalez,[1,2,12,*] Maya E. Kotas,[3] Claire E. O'Leary,[3] Katelyn Singh,[4] William Damsky,[4,5] Chang Liao,[3] Elizabeth Arouge,[1] Iliana Tenvooren,[6] Diana M. Marquez,[6] Andrew W. Schroeder,[3] Jarish N. Cohen,[7] Marlys S. Fassett,[1,2] Jinwoo Lee,[3] Scott G. Daniel,[8] Kyle Bittinger,[8] Roberto Efraín Díaz,[9,10] James S. Fraser,[9] Niwa Ali,[1] K. Mark Ansel,[2] Matthew H. Spitzer,[6,11,12] Hong-Erh Liang,[3] and Richard M. Locksley[2,3,13,14,*]

[1]Department of Dermatology, University of California, San Francisco, San Francisco, CA, USA
[2]Department of Microbiology & Immunology, University of California, San Francisco, San Francisco, CA, USA
[3]Department of Medicine, University of California, San Francisco, San Francisco, CA, USA
[4]Department of Dermatology, Yale School of Medicine, New Haven, CT, USA
[5]Department of Pathology, Yale School of Medicine, New Haven, CT, USA
[6]Department of Otolaryngology and Microbiology & Immunology, University of California, San Francisco, San Francisco, CA, USA
[7]Department of Pathology, University of California, San Francisco, San Francisco, CA, USA
[8]Division of Gastroenterology, Hepatology, and Nutrition, The Children's Hospital of Philadelphia, Philadelphia, PA, USA
[9]Department of Bioengineering and Therapeutic Sciences, University of California, San Francisco, San Francisco, CA, USA
[10]Tetrad Graduate Program, University of California, San Francisco, San Francisco, CA, USA
[11]Parker Institute for Cancer Immunotherapy, San Francisco, CA, USA
[12]Chan Zuckerberg Biohub, San Francisco, CA, USA
[13]Howard Hughes Medical Institute, University of California, San Francisco, San Francisco, CA, USA
[14]Lead contact
*Correspondence: roberto.ricardo-gonzalez@ucsf.edu (R.R.R.-G.), richard.locksley@ucsf.edu (R.M.L.)
https://doi.org/10.1016/j.immuni.2022.08.001

SUMMARY

Demodex mites are commensal parasites of hair follicles (HFs). Normally asymptomatic, inflammatory outgrowth of mites can accompany malnutrition, immune dysfunction, and aging, but mechanisms restricting *Demodex* outgrowth are not defined. Here, we show that control of mite HF colonization in mice required group 2 innate lymphoid cells (ILC2s), interleukin-13 (IL-13), and its receptor, IL-4Ra-IL-13Ra1. HF-associated ILC2s elaborated IL-13 that attenuated HFs and epithelial proliferation at anagen onset; in their absence, *Demodex* colonization led to increased epithelial proliferation and replacement of gene programs for repair by aberrant inflammation, leading to the loss of barrier function and HF exhaustion. Humans with rhinophymatous acne rosacea, an inflammatory condition associated with *Demodex*, had increased HF inflammation with decreased type 2 cytokines, consistent with the inverse relationship seen in mice. Our studies uncover a key role for skin ILC2s and IL-13, which comprise an immune checkpoint that sustains cutaneous integrity and restricts pathologic infestation by colonizing HF mites.

INTRODUCTION

Type 2 immunity is orchestrated by the production of canonical cytokines, such as interleukin-4 (IL-4), IL-5, and IL-13, that are induced during allergic inflammation or infection by parasitic helminths (Gause et al., 2020). Although host-adaptive type 2 immunity engages and typically dominates these chronic afflictions, work over the last decade has revealed innate immune cells, particularly group 2 innate lymphoid cells (ILC2s), as key sources of initial type 2 cytokines in involved tissues. ILC2s develop first during fetal hematopoiesis and position in tissues where they expand perinatally and express effector cytokines like IL-5 and IL-13 at birth (Schneider et al., 2019). Prevalent at mucosal barriers, ILC2s are also in skin (Kobayashi et al., 2019; Ricardo-Gonzalez et al., 2018), where roles in tissue repair have been demonstrated after injury or bacterial invasion (Sakamoto et al., 2021), although contributions of intermittently or constitutively produced type 2 cytokines to basal physiology remain poorly understood.

While investigating an acquired inflammatory skin condition among type 2 immunodeficient mice in the specific pathogen-free (SPF) animal facility at University of California San Francisco (UCSF), we identified a critical role for innate type 2 immunity involving ILC2s in sustaining skin homeostasis in the presence of otherwise benign commensalism by *Demodex*. *Demodex* mites have co-evolved over millions of years as obligate commensal ectoparasites inhabiting the hair follicles (HFs) and sebaceous glands of mammals (Palopoli et al., 2015; Thoemmes et al., 2014). Relatively short-lived (2–3 weeks), the minute arthropods eat sebum and keratinocyte debris and produce 1–2 dozen

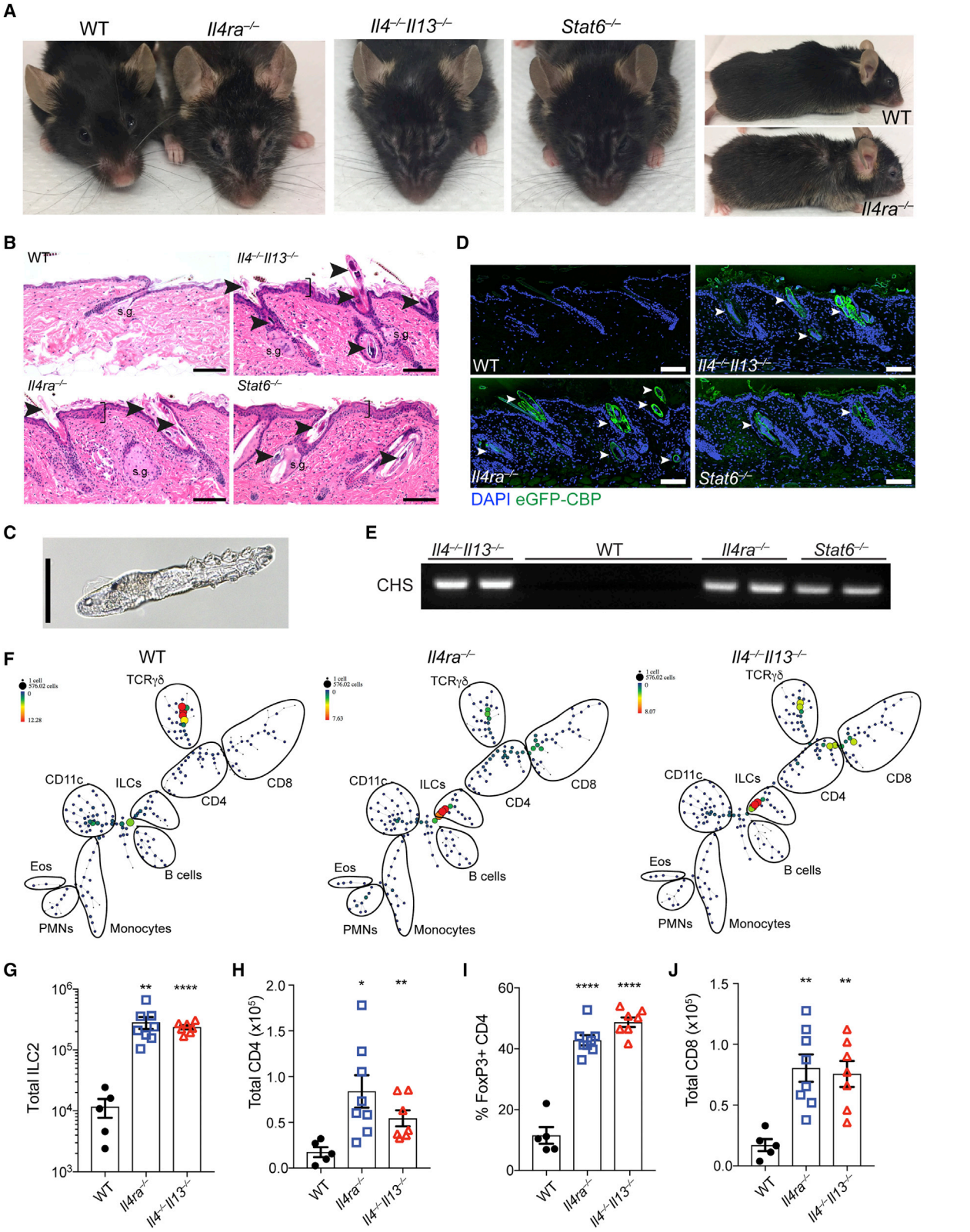

Figure 1. Loss of type 2 immunity results in dermatitis associated with *Demodex* infestation

(A) Representative facial and fur phenotype of wild-type (WT), *Il4ra*$^{-/-}$, *Il4*$^{-/-}$*Il13*$^{-/-}$, and *Stat6*$^{-/-}$ mice at homeostasis. Mice shown are retired male breeders at 18–20 months of age.

(legend continued on next page)

eggs that differentiate through intermediate larvae to generate progeny that spread to nearby follicles unless constrained by undefined host factors (Rather and Hassan, 2014). Among humans, prevalence of asymptomatic *Demodex* commensalism, particularly on the face, reaches essentially 100% with age, but outgrowths can be provoked by skin damage, immunodeficiency, and malnutrition and have been associated with rosacea (Georgala et al., 2001; Zhao et al., 2010), prompting the addition of anti-mite treatment in patients afflicted with inflammation in the setting of a high *Demodex* burden. Clinically, inflammation of the eyelids (blepharitis, which may overlap with ocular rosacea) observed in patients treated with anti-IL-4Ra for atopic dermatitis (Barbé et al., 2021; Simpson et al., 2016) is associated with increased *Demodex spp.* infestation involving the dense HF landscape of the eyelid (Heibel et al., 2021; Quint et al., 2020), suggesting that inhibition of basal IL-4Ra signaling might precipitate *Demodex* overgrowth and HF inflammation.

Using genetic models of adaptive and innate immunity in combination with co-housing and cell transfer experiments, our studies show that loss of type 2 cytokine signaling underlies failure to control HF colonization by *Demodex*. Patients with rhinophymatous rosacea, an inflammatory dermopathy of the nose associated with heavy *Demodex* infestation, had increased HF inflammation but reduced IL-13 as compared with HF incidentally commensalized by *Demodex* among patients without rosacea. Finally, we reveal an unanticipated role for ILC2s and IL-13 in HF and cutaneous homeostasis after perturbation that is activated and sufficient for control of this ubiquitous commensal of mammalian skin.

RESULTS

Demodex outgrowth and inflammatory dermopathy occurs in the absence of type 2 cytokine signaling

Around 8–12 weeks after birth, homozygously maintained *Il4ra*$^{-/-}$, *Il4*$^{-/-}$*Il13*$^{-/-}$, and *Stat6*$^{-/-}$ C57BL/6 mice (here designated type 2 immunodeficient) in our SPF facility developed prominent facial folds and blepharitis, with loss of coat pigmentation that progressed with age (Figure 1A). Microscopic examination of the skin from these type 2 immunodeficient mouse strains revealed acanthosis (thickening of the epidermis), aberrant HF morphology, and enlarged sebaceous glands (Figure 1B). We also observed increased proliferation and numbers of HF stem cells (HFSCs) and increased numbers of HFs (Figures S1A–S1D).

These alterations were accompanied by infestation with HF-dwelling mites with characteristics of *Demodex* species (Figure 1B). We used morphologic criteria of mites from hair pluck specimens (Figure 1C) and sequencing of the 18S ribosomal RNA gene to identify the mites as *Demodex musculi* (Table S1), a relative of human-associated *Demodex folliculorum*. To localize mites by their chitinous exoskeleton, we generated an enhanced GFP chitin-binding domain protein (eGFP-CBP) and examined involved skin using immunofluorescence (IF). We observed mites, often multiple, in essentially all HF and sebaceous glands of back skin in type 2 immunodeficient mice (Figure 1D). To assess the *Demodex* burden, we developed a PCR assay for the highly conserved *Demodex* chitin synthase (CHS) gene (Zhao et al., 2012). Affected type 2-deficient mice were PCR positive, whereas separately maintained, microscopically negative wild-type (WT) mice were PCR negative (Figure 1E). Thus, mice genetically lacking diverse arms of type 2 immunity developed uncontrolled infestation by an otherwise commensal skin ectoparasite, in line with previous reports of infrequent outbreaks of *Demodex* mites in mouse facilities (Smith et al., 2016).

We next sought to understand how immune cells and cytokines were altered in affected mice to explore immune mechanisms necessary for restraining *Demodex* overgrowth. Both flow- and mass cytometry (CyTOF) of immune cells in skin revealed significant expansion of ILC2s, regulatory T (Treg) cells, and CD4^{+} and CD8^{+} T cells in type 2 immunodeficient mice compared with WT C57BL/6 mice (Figures 1F–1J and S1E–S1G). Skin ILC2s were expanded 20-fold to 30-fold in *Demodex*-infected type 2 immunodeficient strains. In prior studies, proliferation of resident ILC2s was shown to drive their extrusion from tissues into the blood (Campbell et al., 2019; Huang et al., 2018; Ricardo-Gonzalez et al., 2020). Consistent with marked expansion of skin ILC2s in the presence of high numbers of mites, skin inflammation in *Demodex-infested* IL4Ra-deficient mice was accompanied by increased circulating ILC2s with the characteristic IL-18R^{+} skin phenotype (Figures S1H and S1I). We also quantified elevated serum IL-5 and IL-13 (in IL-13-sufficient *Il4ra*$^{-/-}$ mice), prototypical ILC2 cytokines (Figure S1J), but also increased serum IL-22 (Figure S1J), suggesting transition of ILC2s to an inflammatory type 2 and type 3 immunophenotype as reported in other contexts (Bielecki et al., 2021; Reynolds et al., 2021). Indeed, skin ILC2s from *Demodex*-infected *Il4ra*$^{-/-}$ mice expressed *Il22* and secreted IL-22 when activated *in vitro* (Figures S1K and S1L). Thus, the absence of type 2 cytokines

(B) Skin sections from WT, *Il4*$^{-/-}$*Il13*$^{-/-}$, *Il4ra*$^{-/-}$, or *Stat6*$^{-/-}$ mice stained with H&E. Arrowheads highlight infestation by *Demodex* mites in hair follicles and sebaceous glands. Brackets emphasize epidermal acanthosis. s.g., sebaceous gland. Scale bars, 100 μm.
(C) Brightfield image of a *Demodex* mite from a fur pluck of *Il4ra*$^{-/-}$ mice. Scale bars, 50 μm.
(D) Skin sections from WT, *Il4*$^{-/-}$*Il13*$^{-/-}$, *Il4ra*$^{-/-}$, or *Stat6*$^{-/-}$ were stained for chitin (green) using an enhanced GFP chitin-binding domain fusion (eGFP-CBP) and DAPI (blue). Arrowheads highlight the *Demodex* mites. Scale bars, 100 μm.
(E) PCR for *Demodex* chitin synthase (CHS) from fur plucks. Images are representative of n ≥ 5 mice of both sexes for each genotype.
(F) SPADE representation of CD45^{+} cells from epidermal fraction of 8–10 weeks old WT, *Il4ra*$^{-/-}$, and *Il4*$^{-/-}$*Il13*$^{-/-}$ mice. One representative plot shown, n = 4 individual mice per genotype.
(G) Number of ILC2s in the skin from WT, *Il4ra*$^{-/-}$, and *Il4*$^{-/-}$*Il13*$^{-/-}$ mice.
(H) Total CD4 in the skin from WT, *Il4ra*$^{-/-}$, and *Il4*$^{-/-}$*Il13*$^{-/-}$ mice.
(I) Frequencies of skin Treg cells (CD3^{+}CD4^{+}FoxP3^{+}, as a percentage of total CD4) in the skin from WT, *Il4ra*$^{-/-}$, and *Il4*$^{-/-}$*Il13*$^{-/-}$ mice at homeostasis.
(J) Total CD8 in the skin from WT, *Il4ra*$^{-/-}$, and *Il4*$^{-/-}$*Il13*$^{-/-}$ mice.
Data are from one representative experiment (F), or pooled from multiple independent experiments (G–J). Data presented as mean ± SEM. *p < 0.05, **p < 0.01, ***p < 0.001, and ****p < 0.0001 by two-tailed Student's t test (versus WT).
Please also see Figure S1.

leads to overgrowth by cutaneous *Demodex*, resulting in lymphocytic infiltrates accompanied by marked ILC2 activation, entry into blood and transition to an inflammatory phenotype.

Human rhinophyma with *Demodex* is associated with folliculitis and reduced *IL13*

The morphologic facial changes observed in infected type 2 immunodeficient mice resembled changes observed in patients affected by rhinophymatous acne rosacea associated with *Demodex* (Forton and Seys, 1993). Rhinophyma is a chronic manifestation of rosacea characterized by acanthosis, inflammation, and enlargement of the sebaceous glands affecting the nose of older adults (Figure 2A). To investigate correlates of the type 2 immune axis in humans that promote stable commensalism with *Demodex*, we analyzed excisions of nasal skin from adults with and without rhinophyma. In normal skin, we identified incidental *Demodex* mite infestation limited to individual HF accompanied by mild inflammatory infiltrates that included more *IL13*- than *IL4*-expressing cells as assessed by RNA *in situ* hybridization (ISH) (Figures 2B–2E). In contrast, patients with rhinophyma had significantly denser inflammatory infiltrates but fewer *IL13*- and *IL4*-expressing cells surrounding HF (Figures 2B–2E). Dual *IL13* ISH and CD3ε immunohistochemistry (IHC) showed that approximately 40% of *IL13*-expressing cells in normal skin were CD3ε negative, consistent with production of this cytokine by both T cells (*IL13*+CD3ε+) and innate lymphocytes (*IL13*+CD3ε−) (Figures 2F and 2G). We also assessed the expression of *IFNG* and *IL22* among these patients for evidence of immune deviation and found that *IFNG* and *IL22* expression was increased in rhinophyma compared with normal skin (Figures 2H–2K). These data show that patients with rhinophyma and *Demodex*, which phenotypically resembles mite infection in type 2 immunodeficient mice, have inflammation and diminished *IL13* production, thus encouraging us to investigate further the mechanisms by which type 2 immunity facilitates stable commensalism by this ubiquitous ectoparasite.

Type 2 immunodeficient mice fail to control HF colonization by *Demodex*

Spontaneous skin inflammation is not typical among type 2 immunodeficient strains in SPF facilities. When affected IL-4Ra-deficient mice were re-derived and bred in separate SPF rooms, none developed dermopathy, skin ILC2 expansion, or *Demodex* infection (Figures 3A, 3G, and 3H). After housing with mite-infested IL-4Ra-deficient mice, however, unaffected IL-4Ra-deficient mice were colonized with *Demodex* and developed both the dermopathy and the immune phenotypes described above over a period of 6–12 weeks (Figures 3B–3G).

To further examine transmissibility, we bred uninfected WT mice to *Demodex*-infected *Il4ra*$^{-/-}$ mice, which were maintained as homozygotes, and subsequently intercrossed the phenotypically normal-appearing heterozygous F1 littermates to generate WT, heterozygous (*Il4ra*$^{+/-}$), and homozygous *Il4ra*$^{-/-}$ F2 mice. Although the F2 generation was derived from previously affected animals, neither WT, heterozygous, nor genetically ablated (*Il4ra*$^{-/-}$) littermates developed the facial or skin inflammation phenotypes when derived from unaffected heterozygous parents descendent from an affected *Il4ra*$^{-/-}$ grandparent (Figures S2A–S2E). However, F1 *Il4ra*$^{-/-}$ mice derived from the intercross of affected *Il4ra*$^{-/-}$ and unaffected heterozygous *Il4ra*$^{+/-}$ mice developed the inflammatory phenotype (Figure S2F), suggesting that direct parental transfer of mites from and to type 2 immunodeficient offspring is important for development of this phenotype. Appearance of the skin and facial phenotypes was accompanied by increases in skin ILC2s, CD4^{+} T cells, and Treg cells, as well as the presence of IL-13 and IL-22 in serum and an increase in follicular mites (Figures S2G–S2O). Thus, under these conditions, functional type 2 immunity, even in heterozygous genotypes, suppresses *Demodex* below what is required for transmission and progression to outgrowth and dermopathic phenotypes in offspring.

Targeted anti-mite but not anti-bacterial therapy prevents the inflammatory dermopathy

Loss of skin ILCs leads to sebaceous gland hypertrophy with altered sebum constituents and effects on the skin bacterial microbiota (Kobayashi et al., 2019). To this end, we performed 16S rDNA amplicon sequencing of skin samples from uninfected WT and *Demodex*-infected and -uninfected *Il4ra*$^{-/-}$ mice (Figure S3A). Although bacterial diversity was similar between phenotypes, analysis of weighted UniFrac distance between samples showed differences in overall community composition (Figure S3B, $p = 0.001$, permutational multivariate ANOVA (PERMANOVA) test). Looking at the broad characteristics of the bacteria, we found that the fraction of obligate anerobes was higher in uninfected mice ($p = 0.028$, Figure S3C), consistent with the normal anerobic environment of the healthy HF (Chen et al., 2018). Despite these microbiota differences, treatment of infected *Il4ra*$^{-/-}$ mice with broad-spectrum antibiotics had no effect on the phenotype (Figure S3D). In contrast, treatment of 6-week-old infected *Il4ra*$^{-/-}$ littermates (before they show the visual phenotype) with topical anti-mite agents moxidectin and imidacloprid (Nashat et al., 2018), but not vehicle control (ethanol), decreased the mite burden and prevented the skin phenotype, in association with reductions in skin ILC2s and normalization of CD4^{+} T cells and Treg cells (Figures S4A–S4G). We obtained comparable results when treating young (4–5 weeks) *Demodex*-infected *Il4*$^{-/-}$*Il13*$^{-/-}$ mice (Figures S4H–S4P). Taken together, these data show that targeted anti-mite therapy reverses the immune disruption and prevents the facial phenotype induced by *Demodex* in the absence of type 2 immunity.

Colonization by *Demodex* drives accumulation of activated ILC2s in normal skin

Our data suggested that type 2 cytokine signaling is required to restrict *Demodex* outgrowth and prevent pathology after colonization. Although neither WT nor heterozygous mice develop the inflammatory dermopathy, we used co-housing to ask how ILC2s and type 2 cytokines respond to *Demodex*. To this end, we co-housed 3- to 5-week-old *Il4ra*$^{-/-}$ mice from infected colonies, before they acquired visible inflammation, with uninfected WT mice. Although *Il4ra*$^{-/-}$ mice developed the cutaneous and facial phenotype with age, as expected, co-housed WT mice remained visually unaffected (Figure 4A). Although *Demodex*-free at the start of co-housing, however, WT mice were colonized by low numbers of mites as established by histologic examination, eGFP-CBP IF, and PCR for *Demodex* CHS

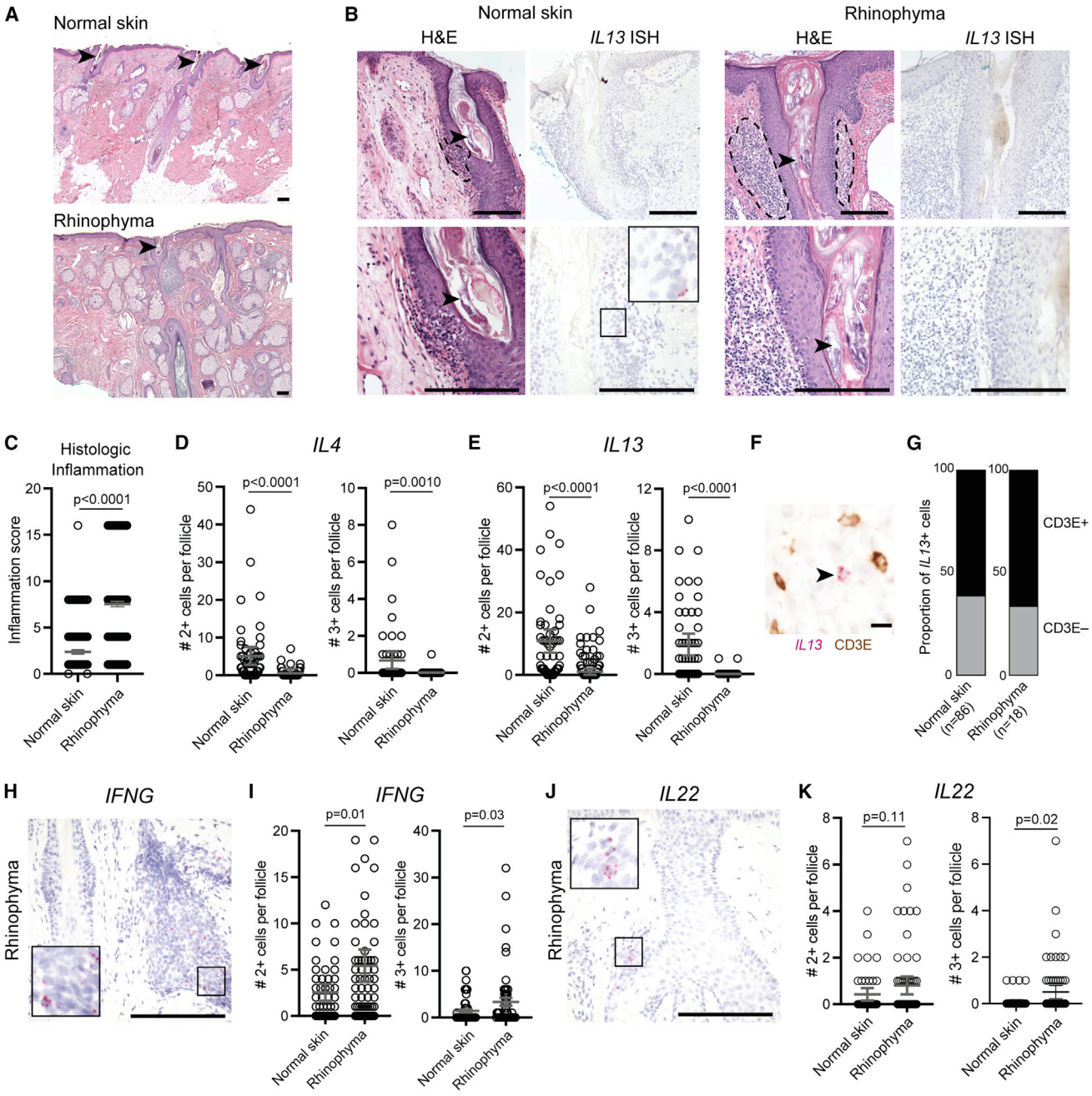

Figure 2. Type 2 cytokines expression is associated with healthy *Demodex* commensalism in humans

(A) Low power H&E-stained sections of normal skin (top) and rhinophyma (bottom).

(B) H&E-stained sections (left panels) and corresponding *IL13* mRNA *in situ* hybridization (ISH, right panels) in hair follicles infected with *Demodex* in representative cases of the normal skin and rhinophyma. Arrowheads highlight *Demodex* infection of the hair follicle. Dashed lines highlight perifollicular inflammation. Scale bars, 250 μm.

(C–E) Scoring of hair follicle inflammation (C) and quantification of *IL4* (D) and *IL13* (E) expression by ISH.

(F and G) Representative co-stained section for *IL13* by ISH and CD3ε by immunohistochemistry (F) and quantification of proportion of $CD3^+$ or $CD3^-$ *IL13*-expressing cells (G). Arrowhead highlights $IL13^+CD3^-$ cell. Scale bars, 10 μm.

(H and I) Representative *IFNG* mRNA ISH (H) and quantification of *IFNG* expression (I) in hair follicles infected with *Demodex*.

(J and K) Representative *IL22* mRNA ISH (J) and quantification of *IL22* expression (K) in hair follicles infected with *Demodex*. Scale bars, 250 μm. Data presented as mean ± SEM. Statistical significance shown by *p < 0.05, **p < 0.01, ***p < 0.001, and ****p < 0.0001 by two-tailed Student's t test.

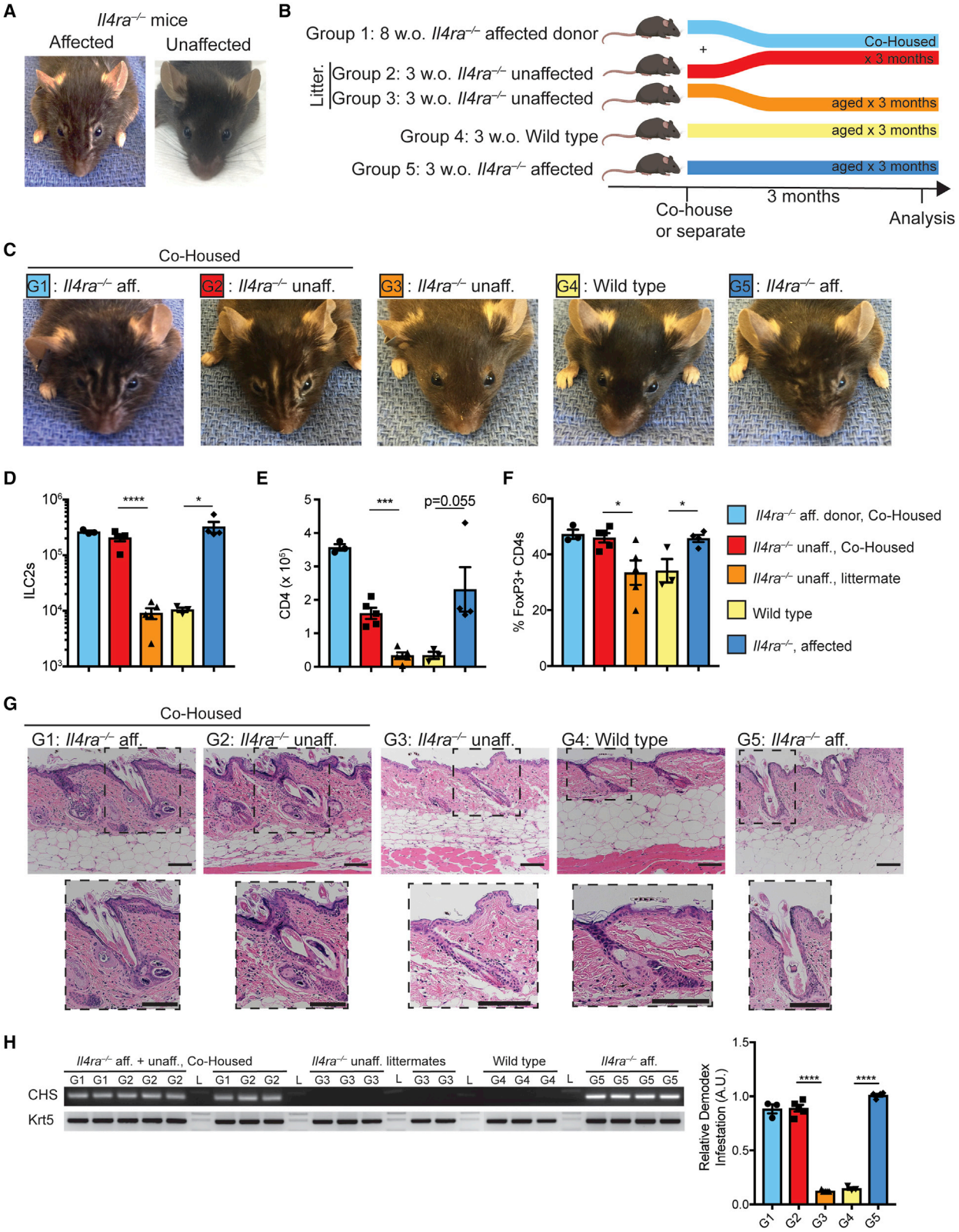

(legend on next page)

(Figures 4B–4D). Infected WT mice developed expansion of skin ILC2s and had increased IL-13 and IL-5 expression in skin, but no cytokines in blood; expansion of activated CD4$^+$ T cells and Treg cells was modest (Figures 4E–4H). Activated skin ILC2s appeared by 2 weeks and peaked 1–2 months after infection of WT mice at approximately half the frequency seen in infected IL-4Ra-deficient mice (Figures 4I–4N). Alarmin cytokines like thymic stromal lymphopoietin (TSLP), IL-25, and IL-33 are important for homeostatic activation of tissue ILC2s; IL-18 may play a similar role in skin (Ricardo-Gonzalez et al., 2018). To assess whether typical alarmins are required for activation of skin ILC2s in response to *Demodex*, we generated *Tslp*$^{-/-}$, *Il18*$^{-/-}$, *Il1rl1*$^{-/-}$, and *Il25*$^{-/-}$ quadruple-ablated (Quad-ablated) mice together with *Il5*^{Red5} and *Il13*^{Smart13} reporters and co-housed the mice with WT and *Demodex*-infected IL-4Ra-deficient mice for 8 weeks. At baseline, Quad-ablated mice had reduced numbers of IL-5- and IL-13-expressing skin ILC2s compared with WT mice (Figures 4O and 4P). Although reduced, skin ILC2s from alarmin-deficient mice retained the proportionate capacity to expand and increase IL-5 and IL-13 in response to mites in association with an attenuated but intermediate *Demodex* burden compared with WT mice and sufficient to block development of the facial phenotype (Figures 4O–4S). Taken together, these data show that *Demodex* colonization provokes expansion and activation of skin ILC2s by a mechanism partially dependent on endogenous alarmins responsible for setting basal innate type 2 immune tone, but absolutely dependent on elaboration of type 2 cytokines to restrict mite outgrowth and attenuate the inflammatory dermopathy.

Although both IL-4 and IL-13 signal through the IL-4Ra receptor, IL-4-deficient mice (*Il4*$^{-/-}$; (Mohrs et al., 2001) controlled *Demodex* as well as WT mice when co-housed with infected IL-4Ra-deficient mice (Figures S5A–S5G), suggesting that IL-13 is necessary for *Demodex* control. We generated IL-13Ra1-deficient mice and co-housed these mice with mite-infected IL-4Ra-deficient mice. *Il13ra1*$^{-/-}$ mice were highly susceptible to *Demodex* outgrowth and developed the dermopathic facial phenotype; heterozygous mice showed partial control (Figures S5H–S5J). We additionally co-housed *Il4*$^{-/-}$ and *Il13ra1*$^{-/-}$ mice with infected mice to demonstrate the requirement for IL-13 but not IL-4 for control of HF infestation (Figures S5K–S5N). Taken together, these experiments in mice and observations from human patients support a key role for type 2 immunity and IL-13 acting through the IL-4Ra and IL-13Ra1 receptor in regulating stable HF colonization by skin mites. In the absence of these constituents of type 2 immunity, *Demodex* overgrowth appears to be the key trigger driving inflammation and ILC2 activation, immune deviation, and appearance in blood.

The adaptive immune system is not required to control *Demodex*

In our initial characterization of *Demodex*-infected type 2 immunodeficient strains, we observed expansion of ILC2s as well as adaptive immune cells. To ascertain a necessary role for the adaptive immune system in *Demodex* control, we co-housed infected IL-4Ra-deficient mice with uninfected Rag1-deficient mice, which lack adaptive B and T cells, including Treg cells. Like infected WT mice, Rag1-deficient animals remained visually unaffected and restrained *Demodex* colonization in contrast to co-housed IL-4Ra-deficient mice (Figures S6A–S6D). As in co-housed WT mice, IL-18R$^+$ skin ILC2s expanded in co-housed *Rag1*$^{-/-}$ mice relative to uninfected controls (Figures S6E–S6H). These data suggested a role for innate immune cells in controlling *Demodex* colonization. To explore this hypothesis, we co-housed infected *Il4ra*$^{-/-}$ mice with uninfected *Rag2*$^{-/-}$ mice, which lack B and T cells, and *Rag2*$^{-/-}$*Il2rg*$^{-/-}$ mice, which also lack ILCs. Within 4–6 weeks of co-housing, *Rag2*$^{-/-}$*Il2rg*$^{-/-}$ mice, but not *Rag2*$^{-/-}$ cage mates, developed the characteristic facial phenotype, blepharitis and increased mite burden observed in *Demodex*-infected type 2 immunodeficient mice (Figures 5A–5D). *Demodex*-infected Rag2-deficient mice had minimal epidermal proliferation (Figure 5E), whereas *Rag2*$^{-/-}$*Il2rg*$^{-/-}$ mice developed hyperplasia, hyperkeratosis, and epithelial proliferation. Thus, under these conditions, the adaptive immune system is not required for control of *Demodex* colonization nor for the expansion of skin ILC2s in response to *Demodex*, whereas ILCs are critical for control of mite burden and prevention of the inflammatory dermopathy.

To test the sufficiency of ILC2s, we sorted ILC2s from *Rag1*$^{-/-}$ mice (expressing *Arg1* and *Il5* reporter alleles as described (Bando et al., 2015; Nussbaum et al., 2013) that were co-housed for 1 month with *Demodex*-infected *Il4ra*$^{-/-}$ mice to activate and expand ILC2s *in vivo* (Figure 5F). Primed ILC2s were purified and transferred into *Rag2*$^{-/-}$*Il2rg*$^{-/-}$ mice prior to and at the start of co-housing with affected *Il4ra*$^{-/-}$ mice. After 6 weeks, we detected transferred ILC2s in the reconstituted *Rag2*$^{-/-}$*Il2rg*$^{-/-}$ mice, which had no facial disfigurement, minimal hyperplasia by skin histology, and reduced *Demodex* burden compared with colonized *Rag2*$^{-/-}$*Il2rg*$^{-/-}$ mice that did not receive ILC2s (Figures 5G–5K). Together, these experiments support a fundamental role for skin ILC2s in control of epithelial homeostasis in response to HF colonization by *Demodex*.

Figure 3. Co-housing *Demodex*-infected with non-infected *Il4ra*$^{-/-}$ mice transfers the phenotype

(A) Facial appearance of *Il4ra*$^{-/-}$ mice infected (affected) or uninfected (unaffected) with *Demodex musculi*.

(B) Schematic of the co-housing experiment. 8-week-old *Il4ra*$^{-/-}$ mice infected with *Demodex* (group 1) were co-housed with unaffected 3-week-old *Il4ra*$^{-/-}$ mice (group 2). Unaffected littermates of co-housed mice (group 3) were allowed to age concurrently. WT (group 4) and *Il4ra*$^{-/-}$ from known *Demodex*-infected parents (group 5) were aged as independent controls.

(C) Representative mice at 3 months after the co-housing experiment. G1–G5 indicate experimental groups as outlined in (B).

(D and E) Number of skin ILC2 (D) and CD4$^+$ (E) cells in the back skin.

(F) Frequency of Treg cells (as percentage of total CD4) in the back skin.

(G) Sections from the back skin were stained with H&E. Inset highlights *Demodex* infestation of the hair follicle and sebaceous glands. Scale bars, 100 μm.

(H) PCR for *Demodex* chitin synthase gene (CHS, top) or genomic DNA for the keratin 5 gene (Krt5, bottom) from 2 mm punches of the back skin. Quantification of relative band intensity (CHS/Krt5) is shown on the right.

Data are from one representative experiment of two independent experiments. Data presented as mean ± SEM. Statistical significance shown by *p < 0.05, **p < 0.01, ***p < 0.001, and ****p < 0.0001 by two-tailed Student's t test. Please also see Figures S2, S3, and S4.

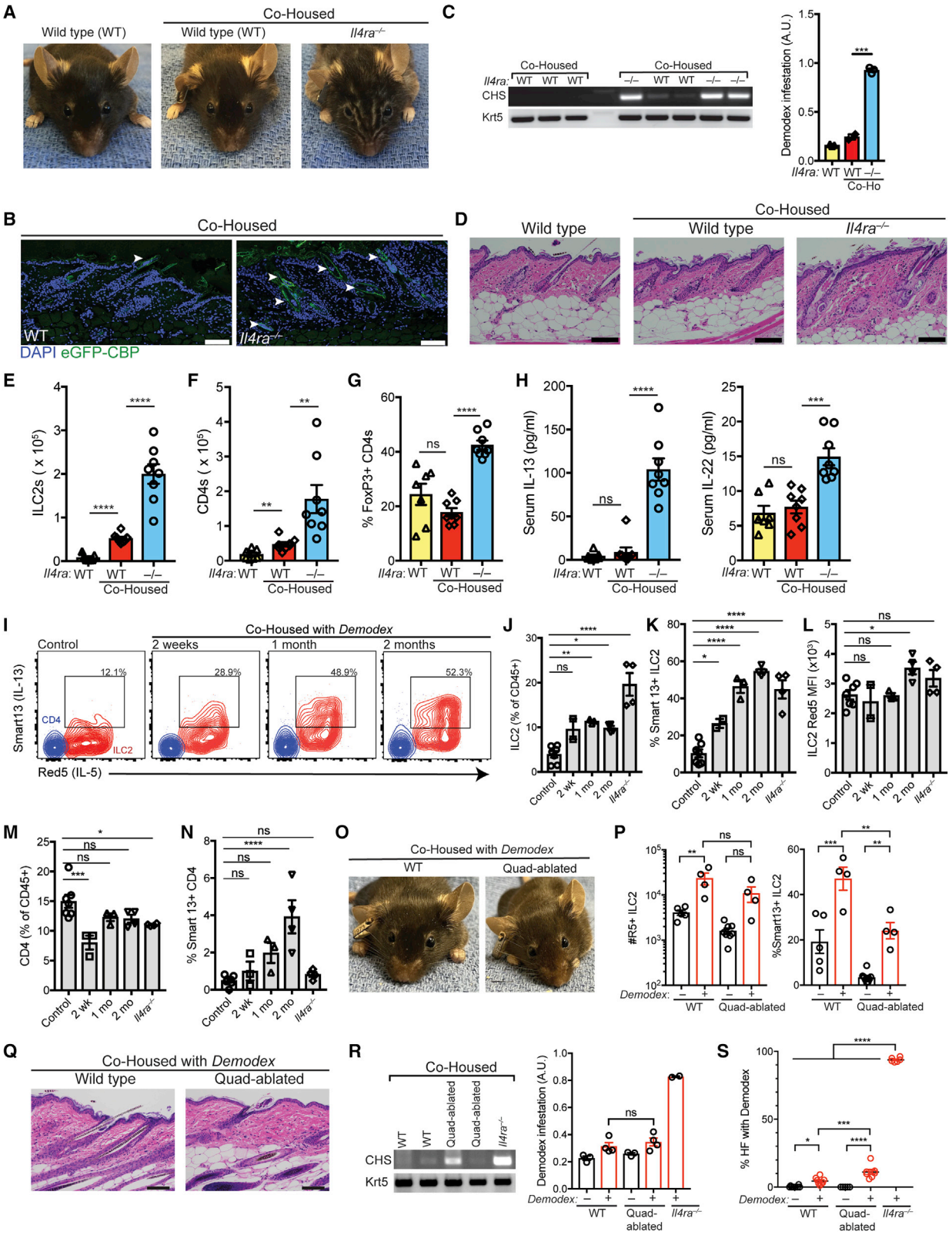

Figure 4. Type 2 immunity sustains non-pathologic *Demodex* colonization

(A) Representative wild-type (WT), and co-housed WT with *Demodex* infested *Il4ra*$^{-/-}$ mice. 3-week-old WT and infested *Il4ra*$^{-/-}$ mice were co-housed for 12 weeks.

(legend continued on next page)

Type 2 immunodeficient mice activate inflammatory rather than repair responses to *Demodex* colonization

To understand the impact of *Demodex* HF colonization on skin homeostasis, we analyzed immune and non-immune cells from type 2 immune-sufficient or -deficient mice infected with *Demodex* using scRNA-seq. In agreement with flow cytometric studies, *Demodex* HF colonization in WT mice led to expansion of IL-18R$^+$ ILC2s (Figures 6A and 6B), which were activated as indicated by expression of *Il13*, *Areg*, and *Il17a* (Figures 6C–6E) and mirroring effector programs associated with tissue repair by skin T cells (Harrison et al., 2019). In type 2 immunodeficient mice, there were increases in ILC2s, Treg cells, and CD8$^+$ T cells, and the appearance of an ILC2-ILC3 transitional population, consistent with our prior findings (Figures 1F–1J, 6F–6H, and S1J–S1L). Of note, skin lymphocytes in infected WT mice mounted an enhanced type 2 immune response, whereas lymphocytes in type 2 immunodeficient strains deviated toward type 1 (*Ifng*) and type 3 (*Il22*) responses (Figures 6H and 6I).

Analysis of CD45$^-$ skin cells from control and *Demodex*-infected WT mice yielded similar representation between the samples among major skin cell populations (Figures S7A and S7B). Gene ontology pathway analysis in *Demodex*-infected WT mice showed induction of pathways associated with extracellular matrix conferring tensile strength, including induction of collagen proteins which were not as highly expressed in *Demodex*-infected *Il4ra*$^{-/-}$ or *Il4*$^{-/-}$*Il13*$^{-/-}$ mice (Figures S7C and S7D). In contrast, infected *Il4ra*$^{-/-}$ and *Il4*$^{-/-}$*Il13*$^{-/-}$ mice revealed induction of pathways associated with host defense and inflammation, response to bacteria (*S100a8*, *S100a9*, *Defb6*, *Stfa1*, and *Srpinb1a*), and antigen presentation (*Tap1*, *H2-M3*, *H2-D1*, *Cd74*, and *H2-Q6*) (Figures S7E and S7F).

To assess skin cells that respond to IL-13, we examined cell populations that expressed *Il4ra, Il13ra1*, or both, noting that the epithelium had a high correlation of *Il4ra* and *Il13ra1* co-expression (Figure S7G). Subclustering and biological processes analyses of the epithelia and *Lgr5*-expressing HFSCs revealed a biological response primed for wound healing in *Demodex*-infected WT mice (Figure S7H). However, this reparative response was absent among epithelia and HFSCs from infected *Il4ra*$^{-/-}$ and *Il4*$^{-/-}$*Il13*$^{-/-}$ mice and replaced by a response characteristic of replicating cells, including DNA synthesis and ribosomal processing (Figures S7I and S7J). Together, these data support a role for the ILC2-IL13 pathway in inducing the restorative and regenerative response necessary to sustain anatomic integrity during colonization by HF mites.

Type 2 cytokines reduce HFSC proliferation and delay HF regrowth

To investigate mechanisms by which IL-13 from ILC2s confers protection of HF after mite colonization, we used well-characterized reporter mice for the type 2 cytokines IL-5 and IL-13 (Liang et al., 2011; Nussbaum et al., 2013) to assess the location and activation of ILC2s in resting skin. ILC2s were the most prevalent cells expressing these cytokines under basal conditions, corroborating prior findings (Mayer et al., 2021; Ricardo-Gonzalez et al., 2018; Schneider et al., 2019), and localized predominantly within the epithelial layer in close association with HF (Figures 7A and 7B). We observed cyclic IL-13 expression in skin ILC2s, with high expression in the early postnatal period as previously observed (Schneider et al., 2019), and then oscillating expression with phases of the hair cycle, which remains synchronous in the first months of life, with low IL-13 during telogen (rest) and high IL-13 during anagen (growth) (Figure 7C). To confirm that cells from IL-13 reporter mice accurately reflect *Il13* gene expression, we sorted ILC2s from back skin of mice in telogen or anagen phases of the hair cycle and confirmed the increase in *Il13* during anagen by quantitative PCR (Figure 7D). These observations suggest that ILC2s and IL-13 may support the cyclic growth and turnover of the HF compartment (Naik et al., 2018), particularly at onset of anagen when this compartment may be susceptible to the 2–3 weeks reproductive cycle of *Demodex*.

To assess the role of type 2 cytokines on hair growth and HFSCs, we depilated mice to induce anagen and synchronous hair regrowth (Ali et al., 2017; Paus et al., 1999) and then administered IL-13 or IL-4, which signal via the common IL-4Ra receptor. Either IL-13 or IL-4, the latter administered as long-lived antibody complexes, slowed hair regrowth (Figures 7E and 7F) and attenuated proliferation of HFSCs (Figures 7G and 7H). We used CyTOF to assess the impact of type 2 cytokine signaling on skin epithelia, which express *Il4ra* and *Il13ra1* (Figure S7G), and observed a decrease in proliferation of the epithelial fraction as assessed by Ki-67 and uptake of the 5-Ethynyl-2′-deoxyuridine (EdU) analog, 5-Iodo-2-deoxyuridine (IdU). IL-4Ra signaling also elicited an increase in phospho-STAT6 (Figures 7I and 7J).

(B) Skin sections from co-housed WT or *Demodex*-infected *Il4ra*$^{-/-}$ were stained for chitin (eGFP-CBP, green) and DAPI (blue). Scale bars, 100 μm.
(C) PCR for *Demodex* chitinase synthase gene (CHS, top) or genomic DNA for the keratin 5 gene (Krt5, bottom) from the back skin. Quantification of relative *Demodex* infestation (CHS/Krt5) is shown on the right.
(D) H&E-stained sections of the back skin from WT, or co-housed WT and *Il4ra*$^{-/-}$ mice. Scale bars, 100 μm.
(E–G) Number of the skin ILC2s (E), total CD4 (F), and frequency of Treg cells (CD3$^+$CD4$^+$FoxP3$^+$ T cells) as a percentage of total CD4 (G).
(H) Quantification of serum IL-13 and IL-22.
(I) IL-5 and IL-13 expression by ILC2s in *Demodex* infection. WT *Il5*$^{tdTomato(Red5)/+}$, *I13*$^{hCD4(Smart13)/+}$ littermates were separated (control) or co-housed with infested *Il4ra*$^{-/-}$ mice (co-housed) for 2 weeks, 1 month, or 2 months. Flow cytometry plots show IL-5 and IL-13 expression by skin ILC2 (red) or CD4 (blue).
(J–L) Quantification of ILC2s (J), and their expression of IL-13 (hCD4, Smart13, K), and IL-5 (L).
(M and N) Quantification of total CD4 (M) and their expression of IL-13 (hCD4, Smart13, N).
(O) Representative wild-type (WT), and *Crlf2*$^{-/-}$, *Il1rl1*$^{-/-}$, *Il18*$^{-/-}$, *Il25*$^{-/-}$ (quad-ablated) mice co-housed with *Demodex* infested *Il4ra*$^{-/-}$ mice.
(P) Number of skin ILC2s and IL-13 expressing (Smart13) ILC2s.
(Q) H&E-stained sections of the back skin from WT, and Quad-ablated mice co-housed with *Demodex*-infected *Il4ra*$^{-/-}$ mice. Scale bars, 100 μm.
(R) PCR for *Demodex* chitinase synthase gene (CHS, top) or genomic DNA for the keratin 5 gene (Krt5, bottom).
(S) Quantification of percentage of hair follicles infected with *Demodex*. Data presented as mean ± SEM. Statistical significance shown by *$p < 0.05$, **$p < 0.01$, ***$p < 0.001$, and ****$p < 0.0001$ by one-way ANOVA.
Please also see Figure S5.

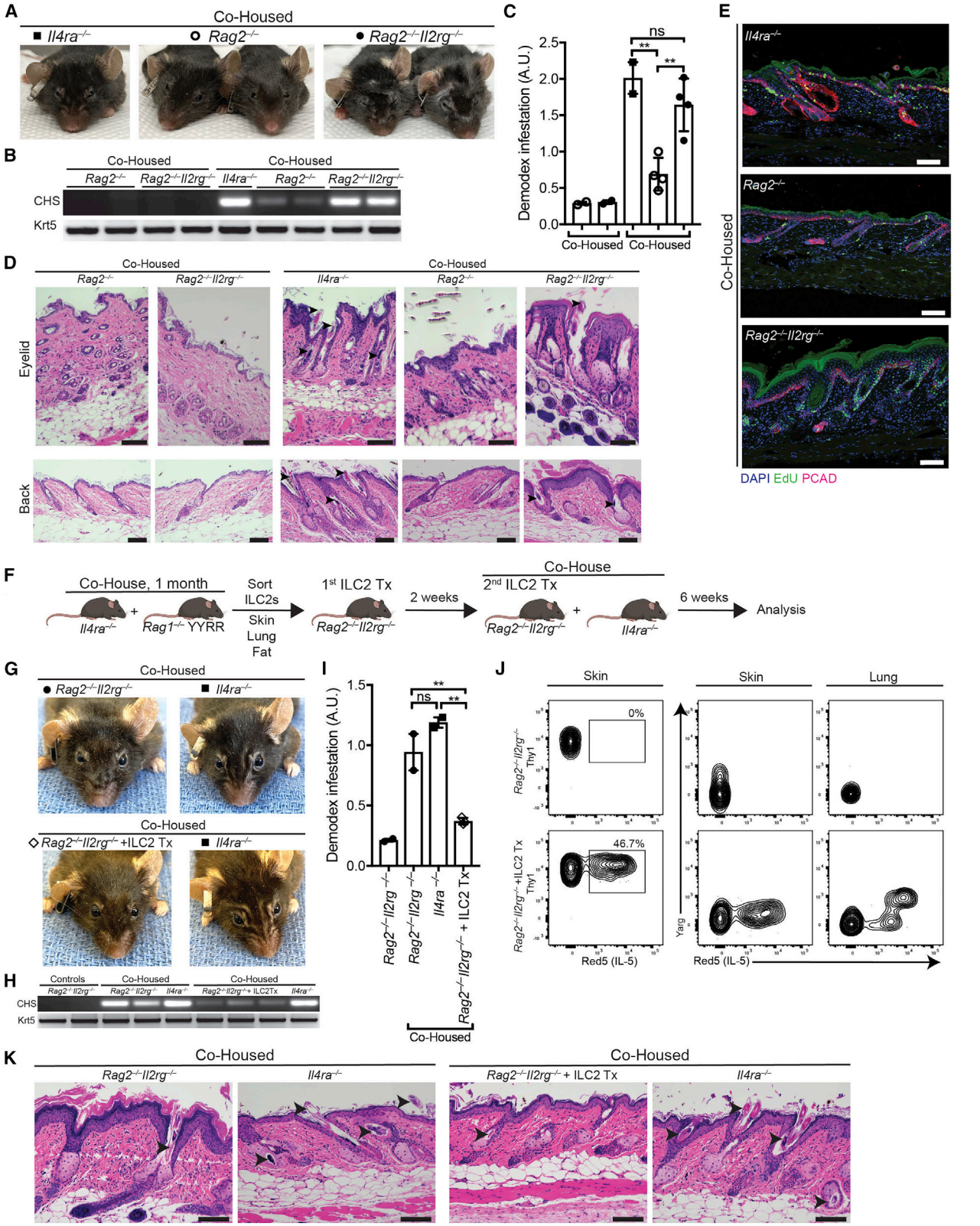

Figure 5. ILC2s are sufficient to restrain *Demodex* infection

(A) Representative *Rag2*$^{-/-}$ and *Rag2*$^{-/-}$*Il2rg*$^{-/-}$ co-housed with *Demodex* infested *Il4ra*$^{-/-}$ mice. 5-week-old *Rag2*$^{-/-}$ and *Rag2*$^{-/-}$*Il2rg*$^{-/-}$ were co-housed with *Demodex* infested *Il4ra*$^{-/-}$ for 6 weeks. n = 3–5 mice per group, representative of two independent experiments.

(legend continued on next page)

These findings, in combination with our scRNA-seq data (Figure S7), support a link between type 2 cytokines, epithelia, and HFs in sustaining skin homeostasis that is evident after colonization by mites.

Loss of type 2 immunity compromises cutaneous integrity in the setting of *Demodex* colonization

The loss of a skin reparative response seen in mite-colonized WT compared with colonized *Il4ra*$^{-/-}$ and *Il4*$^{-/-}$*Il13*$^{-/-}$ mice, together with the loss of the normal obligate anerobes from HF in infected *Il4ra*$^{-/-}$ mice (Figure S3C), led us to hypothesize that type 2 immunity may be necessary to preserve HF and skin integrity in the setting of perturbation. To test this hypothesis, we measured transepidermal water loss (TEWL) in WT, IL-4Ra-deficient and *Demodex*-infected IL-4Ra-deficient mice. We noted barrier dysfunction in *Demodex*-infected IL-4Ra-deficient mice compared with uninfected IL-4Ra-deficient mice (separately housed) or *Demodex*-colonized WT mice (housed in the same cage as affected IL-4Ra-deficient mice) (Figures 7K and 7L). Further, penetration of lucifer yellow applied to *depilated* skin was constrained to the epidermis and upper HF in WT mice but diffused throughout the subcutaneous tissues in IL-4Ra-deficient mice, even in the absence of mite infection (Figure 7M).

The finding that depilation alone was sufficient to reveal loss of skin integrity in the absence of type 2 cytokines led us to hypothesize that the repetitive demands of persistent mite HF colonization on tissue repair might drive the appearance of the inflammatory dermopathy among type 2 immunodeficient mice by exceeding the limits for tissue resilience. To test this, we performed sequential depilations in WT or *Il4*$^{-/-}$*Il13*$^{-/-}$ mice infected with mites. Although WT mice re-grew hair with each cycle as predicted (Paus et al., 1999), *Il4*$^{-/-}$*Il13*$^{-/-}$ mice had increasingly slower kinetics of regrowth with subsequent depilations (Figure 7N). Histologic examination showed that WT mice maintained normal HF morphology and subcutaneous adipose tissue, whereas *Il4*$^{-/-}$*Il13*$^{-/-}$ mice had a more fibrotic dermis and HF structures were further compromised, consistent with alterations accompanying tissue senescence (Figure 7O; Ge et al., 2020). Supporting this, aged *Demodex*-infected type 2 immunodeficient mice developed premature coat depigmentation compared with similarly aged WT mice (Figure 7P). Analyses of HFSCs from 20 to 24 months old, age-matched WT and *Demodex*-infected *Il4*$^{-/-}$*Il13*$^{-/-}$ mice showed an increase of the senescence-associated marker *Cdkn2a/p16* in the absence of type 2 cytokines (Figure 7Q). Taken together, these data reveal a key role for skin ILC2s and innate type 2 immunity in enhancing skin resilience following inflammation in response to HF colonization by *Demodex*.

DISCUSSION

Demodex mites are ubiquitous ectoparasites considered commensals of mammalian HFs (Rosshart et al., 2019; Sastre et al., 2016). As such, *Demodex* outbreaks remain infrequently reported among SPF mice facilities but have been noted among strains deficient in type 2 immunity, as occurred here (Smith et al., 2016). As we have shown by co-housing and transfer experiments, activation of ILC2s, IL-13, and signaling through IL-4Ra were necessary and sufficient to limit proliferation and spread of mites once acquired in the pilosebaceous units of the skin. Further study revealed deficits in the ability of type 2 immunodeficient mice to sustain skin homeostasis not only following mite colonization but also after depilation. Repetitive depilation resulted in evidence for SC failure, and aged type 2 immunodeficient mice colonized with *Demodex* developed skin changes consistent with premature HF senescence, uncovering a non-redundant role for type 2 immunity in sustaining cutaneous integrity in the post-birth environment.

Despite their ubiquitous nature and robust reproductive potential, *Demodex* are maintained at low density on human skin, although mites proliferate in settings of immunodeficiency, malnutrition, and with aging, particularly in sun-exposed areas of the face (Chovatiya and Colegio, 2016; Lacey et al., 2011). Human-associated *Demodex* possess a reductive genome anticipated by obligate parasites that spend their entire life within the narrow niche of HFs. *Demodex* share chitinous exoskeletons with other arthropods, and survival in the sebum-rich HF has evolved a rich armamentaria of lipases, proteases, and chitinases (Hu et al., 2019), an array of enzymes linked, like chitin itself, with tissue injury, alarmin induction, and activation of innate type 2 immunity (Cheng and Locksley, 2014; Gieseck et al., 2018; Van Dyken et al., 2017). As we have shown, loss of canonical alarmins attenuated but did not ablate the ILC2 response, suggesting a prominent role for

(B) PCR for *Demodex* chitinase synthase gene (CHS, top) or genomic DNA for the keratin 5 gene (Krt5, bottom) from the back skin.
(C) Quantification of relative *Demodex* infestation (CHS/Krt5) for the PCR in (B).
(D) H&E-stained sections of eyelid (top) and back (bottom) skin from unaffected *Rag2*$^{-/-}$ and *Rag2*$^{-/-}$*Il2rg*$^{-/-}$ with or without co-housing with a *Demodex* infested *Il4ra*$^{-/-}$.
(E) Sections from the back skin of co-housed *Il4ra*$^{-/-}$, *Rag2*$^{-/-}$ and *Rag2*$^{-/-}$*Il2rg*$^{-/-}$ were stained for EdU (green), P-cadherin (red), and DAPI (blue).
(F) Schematic of the adoptive transfer experiment. *Il4ra*$^{-/-}$ mice infected with *Demodex* were co-housed with unaffected 4- to 8-week-old *Rag1*$^{-/-}$*Arg*$^{YFP/YFP}$, *Il5*$^{tdTomato(Red5)/tdTomato(Red5)}$ (*Rag1*$^{-/-}$ YYRR) mice for 1 month. ILC2s (CD45^{+}Lin^{-}Thy1^{+}Red5^{+}) were sorted from the skin, lungs, and fat, pooled, and transferred to *Rag2*$^{-/-}$*Il2rg*$^{-/-}$ mice 2 weeks prior and at the start of co-housing (see STAR Methods).
(G) Representative *Rag2*$^{-/-}$*Il2rg*$^{-/-}$ treated with PBS (top) or with transferred ILC2s (bottom) after 6 weeks of co-housing with *Demodex*-infected *Il4ra*$^{-/-}$.
(H) PCR for *Demodex* chitinase synthase gene (CHS, top) or genomic DNA for the keratin 5 gene (Krt5, bottom) from the back skin.
(I) Quantification of relative *Demodex* infestation (CHS/Krt5) for the PCR in (H).
(J) Flow cytometry plots of ILCs (pre-gated on Live CD45^{+}Lin^{-}Thy1^{+}) showing IL-5 expression (left panels) or Arginase (middle and right panels) on the skin and lungs as indicated.
(K) H&E-stained sections of the back skin from *Rag2*$^{-/-}$*Il2rg*$^{-/-}$ treated with PBS or ILC2 adoptive transfer and co-housed with *Demodex* infested *Il4ra*$^{-/-}$. n = 3–5 mice per condition. Arrowheads highlight *Demodex* mites. Scale bars, 100 μm. For the ILC2 transfer experiments, a representative mouse is shown from 2 independent experiments with n = 2–3 mice per group. Data presented as mean ± SEM. Statistical significance shown by *p < 0.05, **p < 0.01, ***p < 0.001, and ****p < 0.0001 by one-way ANOVA.
Please also see Figure S6.

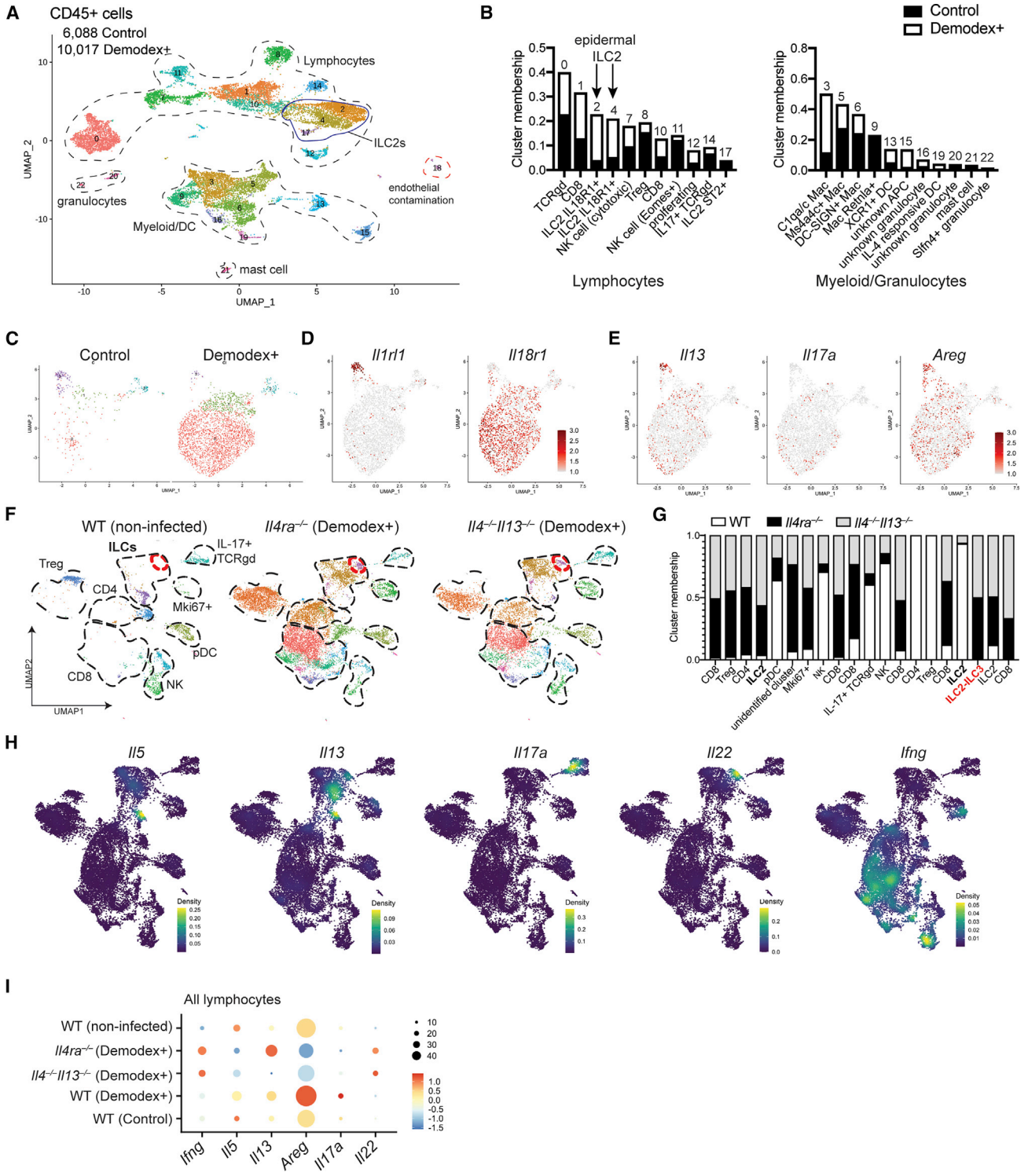

Figure 6. scRNA-seq of CD45$^+$ cells from *Demodex*-infected WT and type 2 immunodeficient mice reveal divergent responses

(A) UMAP projection of CD45$^+$ cells from the skin of WT uninfected and *Demodex*-infected mice.

(B) Bar plot showing the percentage of cells in each cluster for all lymphocyte (left) and myeloid and granulocyte (right) populations by experimental condition.

(C) UMAP projection of ILC subclustering analyses showing experimental condition.

(D) Feature plot of ILC subclusters showing expression of genes associated with ILC2 subset identity in the skin.

(E) Feature plots showing expression of genes for *Il13*, *Il17a*, and *Areg*.

(legend continued on next page)

alarmins in regulating basal ILC2 numbers and tone, but revealing alternative pathways by which ILC2s react to tissue perturbations induced by this evolved HF commensal. Although skin development and basal homeostasis were largely normal in the absence of ILC2s or type 2 cytokines, perturbations like depilation, *Demodex* and aging resulted in dysregulation and loss of barrier function. In concert with additional signals, including via the epidermal growth factor receptor (EGFR), type 2 cytokines impacted small intestinal epithelial SC trajectories, hinting at shared pathways by which type 2 immunity can enhance resilience to perturbations at cutaneous and mucosal barriers (Sanman et al., 2021). Such adaptations in the gut contribute to the phenomenon of concomitant immunity by which helminth-infected hosts become resistant to further infestation by immature forms (Schneider et al., 2018). Whether HF colonization by *Demodex* imparts similar SC and epithelial "memory" and protection against subsequent cutaneous injury will be important areas for further investigation (Gonzales et al., 2021).

Our studies suggest a role for IL-13 in transiently restraining HFSC and epithelial proliferation at anagen onset, revealing barrier abnormalities upon depilation in the absence of this cytokine. Perturbations that impact the skin HF niche by disruptions of cell junctions, migration, and adhesion, pathways we show engaged by *Demodex* colonization, drive precocious anagen entry, resulting in re-directed proliferation of HFSCs toward "rescue" states dedicated to preservation of the HF niche (Gur-Cohen et al., 2019; Harrison et al., 2019; Lay et al., 2018). Precocious anagen entry would be compatible with the increased numbers of proliferating HFSCs and HFs observed in mite-colonized type 2 immunodeficient mice. Of note, the epithelial and HFSC reparative pathways induced by IL-13 in naive and mite-colonized WT animals were lost in type 2 immunodeficient mice and replaced by epithelial proliferation and an inflammatory cell influx that was not sufficient to control infestation. Given the marked HF anatomic complexities occurring among epithelial and endothelial structures during the transition through anagen (Yang et al., 2017), it is tempting to speculate that effects of IL-13 are critical to keep *Demodex* compartmentalized to regions of the HF above the isthmus, compared with the deeper localization of organisms seen in type 2 immunodeficient mice. ILC2s in intestinal mucosa regulate homeostasis with the protozoan, *Tritrichomonas* (Howitt et al., 2016; Schneider et al., 2018), suggesting a role for innate type 2 immune cells in sustaining tissue function in the presence of barrier-associated eukaryotic pathobionts, perhaps reflecting responsiveness of ILC2s to endogenous damage-associated molecular patterns (DAMPs) rather than to genetically encoded microbial and viral recognition elements. Although we cannot exclude a role for microbiota-mediated inflammation contributing to the inflammatory phenotype, the infection was controlled by topical drugs targeting the mite but not by antibiotics.

Our observations of increased type 2 inflammation in mite-colonized type 2 immunodeficient mice were bolstered by evidence for increased inflammation but diminished IL-4 and IL13-producing innate immune cells among patients with rhinophymatous rosacea associated with *Demodex*. We cannot exclude contributions by adaptive or unconventional T cells that produce IL-13, particularly with the presence of such cells in human rhinophyma samples under non-SPF conditions with longer life experience as compared with mice. It is possible that the increased prevalence of atopy in the aging population, and perhaps even the early age of onset of type 2 inflammation in atopic skin disease, might represent physiologic efforts to promote tissue integrity and homeostasis during stress induced by senescence and growth, respectively. Efforts to understand the role of traditional immune cells in "physiological" inflammation will be important to anticipate responses to prevalent biologic therapeutics, particularly in aging populations (Medzhitov, 2021). The availability of potent biologics inhibiting type 2 immunity that require continuous therapy may benefit from targeted screening of high-risk patients to curtail symptomatic blepharitis and other cutaneous eruptions while potentially optimizing long-term tissue integrity, particularly in the setting of high *Demodex* burden.

Limitations of the study

We characterized an inflammatory dermopathy caused by *Demodex* among mice at UCSF. Although cases have been noted elsewhere (Smith et al., 2016), the impact of local microbial flora and animal care practices remain unstudied. We analyzed a small human cohort to provide corroborative evidence, but further studies are needed across more diverse patient groups to assess the generalizable nature of these findings. Humans are colonized with two types of *Demodex* and the periodicity of anagen and telogen in humans differs from mice. Although *Demodex* outgrowths have been noted among patients treated with anti-IL4Ra, controlled trials are needed to assess potential causality linking these drugs with cutaneous outcomes related to *Demodex*. Finally, increasing information regarding *Demodex* genomes (Smith et al., 2022) may facilitate identification of moieties or metabolites that sustain quiescent colonization that might represent the target of IL-13-induced host molecules that enable the widespread and successful habitation of the HF niche by these creatures.

STAR★METHODS

Detailed methods are provided in the online version of this paper and include the following:

- KEY RESOURCES TABLE
- RESOURCE AVAILABILITY
  - Lead contact
  - Materials availability
  - Data and code availability

(F) UMAP projection of the skin lymphocyte fraction of WT (uninfected), and *Il4ra*$^{-/-}$ or *Il4*$^{-/-}$*Il13*$^{-/-}$ (*Demodex*-infected) mice showing subset of lymphocytes. Red circle denotes ILC2-ILC3 population present only in *Il4ra*$^{-/-}$ or *Il4*$^{-/-}$*Il13*$^{-/-}$ samples.
(G) Bar plot showing the percentage of cells in each cluster for the samples in (F).
(H) Density plots from the combined object as in (F), showing the expression for selected cytokines. (I) Dot plot of a combined analysis for all lymphocytes in all samples.
Please also see Figure S7.

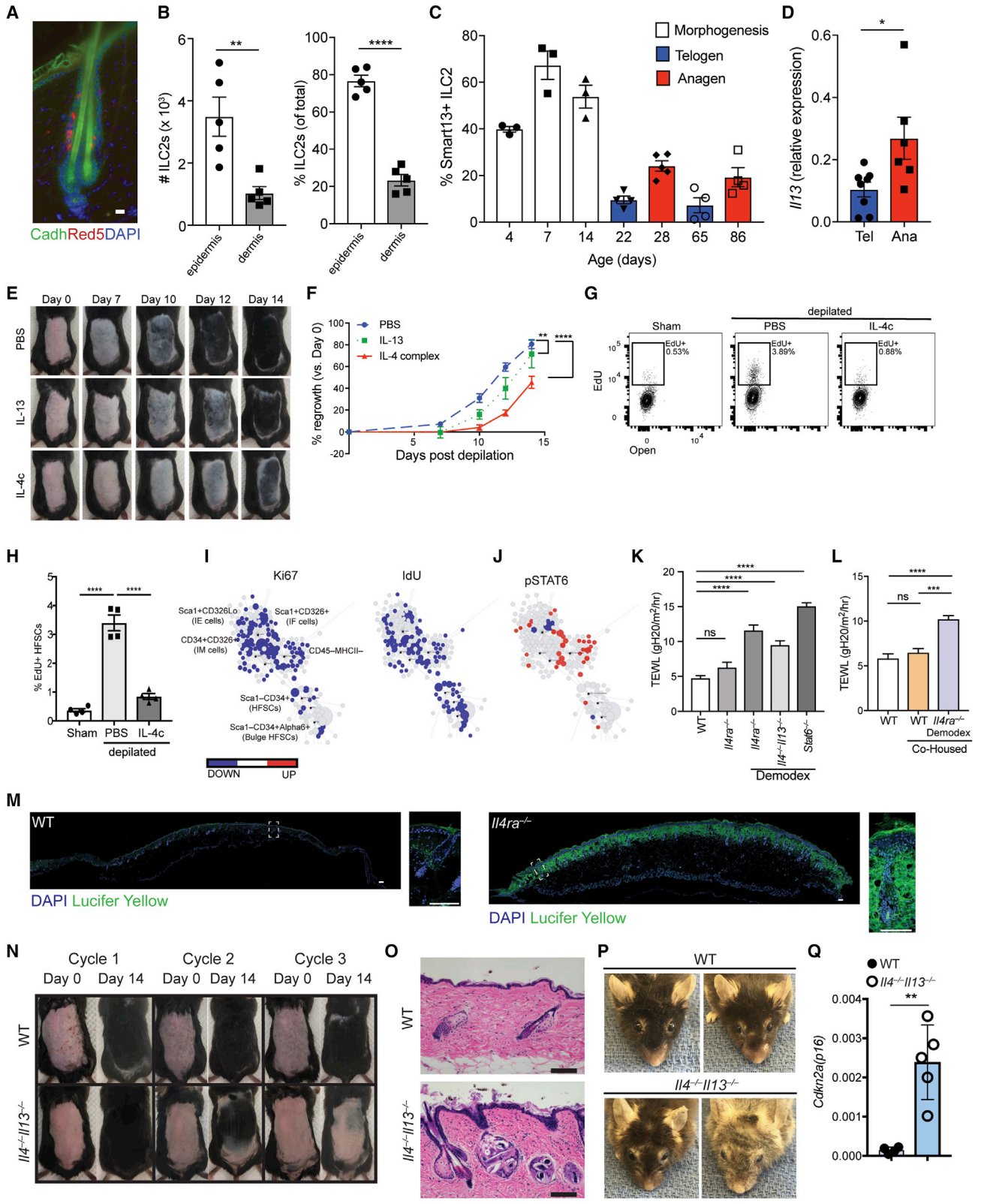

Figure 7. Type 2 immunity sustains skin barrier and HF regeneration after perturbation

(A) Localization of IL-5 producing ILC2s (red) within the skin epithelium. E-cadherin (green) is used to highlight hair follicles. DAPI is represented in blue. Scale bars, 20 μm.

(legend continued on next page)

SUPPLEMENTAL INFORMATION

Supplemental information can be found online at https://doi.org/10.1016/j.immuni.2022.08.001.

ACKNOWLEDGMENTS

We thank M. Ji and M. Conseco for technical expertise and mouse colony maintenance, Z. Wang for cell sorting, J. Bolen and X.Y. Jiang and the UCSF Biomarkers and Histology Core for assistance with histology. We thank members of the Locksley laboratory and M.D. Rosenblum, A.L. DeFranco, J. von Moltke, and C. Schneider for comments on the manuscript. Figure diagrams were created with BioRender.

This work was supported by the National Institutes of Health (AR007175 to R.R.R.-G. and M.S.F., AR075880 to R.R.R.-G., HL140868 to M.E.K., DK121476 to C.E.O., AI159229 to W.D., AR074556 to M.S.F., and AI026918 and HL107202 to R.M.L.), Dermatology Foundation (R.R.R.-G. and M.S.F.), A.P. Giannini Foundation (R.R.R.-G. and M.E.K.), Robert Wood Johnson Foundation (R.R.R.-G.), Howard Hughes Medical Institute (R.M.L.), University of California Tobacco-Related Disease Research Program (T29IP0554 to J.S.F.), and the Sandler Asthma Basic Research Center at the University of California San Francisco. R.E.D. was supported by NSF GRFP (#1650113). R.E.D. is a Howard Hughes Medical Institute Gilliam Fellow (#GT11377). R.R.R.-G. and M.H.S. are Chan Zuckerberg Investigators.

AUTHOR CONTRIBUTIONS

R.R.R.-G. conceived the study, designed and performed experiments, analyzed and interpreted the data, and wrote the manuscript. M.E.K., H.-E.L., C.E.O., C.L., E.A., and J.L. participated in performing experiments, provided intellectual expertise, and/or helped to interpret experimental results. C.L. and H.-E.L. generated the IL-13Ra1-deficient mice. I.T. and D.M.M. performed CyTOF analyses on skin samples under the supervision and guidance of M.H.S. K.S. and W.D. performed and analyzed the RNAscope experiments on human tissue samples. J.N.C. assisted with the initial histologic examination of *Demodex* and TEWL experiments. M.S.F. and K.M.A. provided mice for co-housing experiments. S.G.D. and K.B. contributed to 16S sequencing analysis. A.W.S. and C.E.O. contributed to the analyses of scRNA-seq data. R.E.D. and J.S.F. designed, expressed, and purified the eGFP-CBP fusion protein. N.A. assisted with experiments related to analysis of HF cycling, and epithelial and SC compartments. R.M.L. directed the studies, analyzed and interpreted data, and wrote the paper with R.R.R.-G. with input from the co-authors.

DECLARATION OF INTERESTS

R.M.L. is a member of the Scientific Resource Board at Genentech and serves on the Advisory Board at Immunity.

INCLUSION AND DIVERSITY

One or more of the authors of this paper self-identifies as an underrepresented ethnic minority in science. One or more of the authors of this paper received support from a program designed to increase minority representation in science.

Received: March 1, 2022
Revised: June 27, 2022
Accepted: August 2, 2022
Published: August 30, 2022

(B) Quantification (left) or percentage (right) of ILC2s ($CD45^+Lin^-Thy1^+Red5^+$) in the epidermis and dermis of adult $Il5^{Red5/+}$ mice.
(C) Quantification of expression of IL-13 by ILC2s throughout the various stages of the hair follicle cycle.
(D) Quantitative PCR for *Il13* expression by ILC2s ($CD45^+Lin^-Thy1^+Red5^+$) sorted from the mice back skin in telogen or anagen stage of the hair cycle.
(E) Effect of IL-4 and IL-13 subcutaneous injection in hair growth. Wild-type C57BL/6 mice were treated with PBS, IL-13, or IL-4 complex (IL-4c) on the first 2 days after depilation (days 0 and 1) and their hair regrowth pattern was tracked over 2 weeks. One representative mouse per treatment arm is shown.
(F) Quantification of hair regrowth from PBS, IL-4c, or IL-13 treated mice as in (E).
(G) Representative flow cytometry panel of hair follicle stem cells (HFSCs, pre-gated as $CD45^-MHCII^-CD34^+Alpha6^+$) incorporation of EdU. Mice were depilated and treated with IL-4 complex (IL-4c) on the first 2 days after depilation. Mice were harvested on day 4 after depilation.
(H) Percent EdU^+ HFSCs 4 days after depilation as in (G).
(I) Scaffold maps of Ki67 and IdU for the $CD45^-$ epidermal cell fraction as analyzed by CyTOF (see STAR Methods). Black nodes represent canonical cell populations identified manually as noted in the top left scaffold map. Blue denotes the population has significant lower expression frequency of the marker (Ki67, or IdU, as denoted in the columns) in the experimental arm (IL-4 complex treated WT mice) versus WT controls; red denotes significantly higher frequency. n = 4 individual mice per group.
(J) Scaffold maps for phospho(p)STAT6 in IL-4 complex treated mice compared with WT controls. Blue and red colors denote statistically significant decrease or increase in expression frequency, respectively, in each cluster compared with the control group ($q < 0.05$ by SAM).
(K) Transepidermal water loss at homeostasis in WT, $Il4ra^{-/-}$ and *Demodex*-infested $Ilra4^{-/-}$, $Il4^{-/-}Il13^{-/-}$, and $Stat6^{-/-}$ mice.
(L) Transepidermal water loss at homeostasis in WT or WT mice co-housed with *Demodex*-infested $Il4ra^{-/-}$ mice.
(M) Lucifer yellow barrier assay. WT or $Il4ra^{-/-}$ were shaved and depilated. 2 days post-depilation, the epidermal surface was exposed to lucifer yellow overnight at 37°C. Lucifer yellow in green, DAPI in blue. Scale bars, 100 μm.
(N) Repeated depilation of wild-type (WT) and $Il4^{-/-}Il13^{-/-}$ mice. A representative animal from n = 4 individual mice shown.
(O) Sections from the back skin of WT and $Il4^{-/-}Il13^{-/-}$ mice after 3 cycles of depilation were stained with H&E. Scale bars, 100 μm.
(P) Representative images of 2-year-old WT and $Il4^{-/-}Il13^{-/-}$ mice.
(Q) qPCR for *Cdkn2a(p16)* from sorted HFSCs from age-matched 2-year-old WT and $Il4^{-/-}Il13^{-/-}$ mice.
Data presented as mean ± SEM and are representative of at least two independent experiments with $n \geq 3$ mice per individual group/time point, pooled from two independent cohorts with n = 5–10/group (K and L) or representative from an experiment with $n \geq 4$ per group (P and Q). *$p < 0.05$, **$p < 0.01$, ***$p < 0.001$, and ****$p < 0.0001$ as calculated with two-tailed Student's t test (A–D and Q) or ANOVA (F, H, K, and L).

REFERENCES

Ali, N., Zirak, B., Rodriguez, R.S., Pauli, M.L., Truong, H.A., Lai, K., Ahn, R., Corbin, K., Lowe, M.M., Scharschmidt, T.C., et al. (2017). Regulatory T cells in skin facilitate epithelial stem cell differentiation. Cell *169*, 1119–1129.e11.

Anderson, M.J. (2001). A new method for non-parametric multivariate analysis of variance. Austral Ecol. *26*, 32–46.

Bair, E., and Tibshirani, R. (2004). Semi-supervised methods to predict patient survival from gene expression data. PLoS Biol. *2*, E108.

Bando, J.K., Liang, H.E., and Locksley, R.M. (2015). Identification and distribution of developing innate lymphoid cells in the fetal mouse intestine. Nat. Immunol. *16*, 153–160.

Bando, J.K., Nussbaum, J.C., Liang, H.E., and Locksley, R.M. (2013). Type 2 innate lymphoid cells constitutively express arginase-I in the naive and inflamed lung. J. Leukoc. Biol. *94*, 877–884.

Barbé, J., Poreaux, C., Remen, T., Schoeffler, A., Cloché, V., Schmutz, J.L., Escobar, G., and Busztejn, A.C. (2021). Prevalence of ocular disease during dupilumab treatment for atopic dermatitis: a bicentric retrospective comparative cohort study. Int. J. Dermatol. *60*, 1520–1528.

Behbehani, G.K., Thom, C., Zunder, E.R., Finck, R., Gaudilliere, B., Fragiadakis, G.K., Fantl, W.J., and Nolan, G.P. (2014). Transient partial permeabilization with saponin enables cellular barcoding prior to surface marker staining. Cytometry A *85*, 1011–1019.

Bielecki, P., Riesenfeld, S.J., Hütter, J.C., Torlai Triglia, E., Kowalczyk, M.S., Ricardo-Gonzalez, R.R., Lian, M., Amezcua Vesely, M.C., Kroehling, L., Xu, H., et al. (2021). Skin-resident innate lymphoid cells converge on a pathogenic effector state. Nature *592*, 128–132.

Bokulich, N.A., Kaehler, B.D., Rideout, J.R., Dillon, M., Bolyen, E., Knight, R., Huttley, G.A., and Gregory Caporaso, J. (2018). Optimizing taxonomic classification of marker-gene amplicon sequences with QIIME 2's q2-feature-classifier plugin. Microbiome *6*, 90.

Bolyen, E., Rideout, J.R., Dillon, M.R., Bokulich, N.A., Abnet, C.C., Al-Ghalith, G.A., Alexander, H., Alm, E.J., Arumugam, M., Asnicar, F., et al. (2019). Reproducible, interactive, scalable and extensible microbiome data science using QIIME 2. Nat. Biotechnol. *37*, 852–857.

Bruggner, R.V., Bodenmiller, B., Dill, D.L., Tibshirani, R.J., and Nolan, G.P. (2014). Automated identification of stratifying signatures in cellular subpopulations. Proc. Natl. Acad. Sci. USA *111*, E2770–E2777.

Callahan, B.J., McMurdie, P.J., Rosen, M.J., Han, A.W., Johnson, A.J., and Holmes, S.P. (2016). DADA2: high-resolution sample inference from Illumina amplicon data. Nat. Methods *13*, 581–583.

Campbell, L., Hepworth, M.R., Whittingham-Dowd, J., Thompson, S., Bancroft, A.J., Hayes, K.S., Shaw, T.N., Dickey, B.F., Flamar, A.L., Artis, D., et al. (2019). ILC2s mediate systemic innate protection by priming mucus production at distal mucosal sites. J. Exp. Med. *216*, 2714–2723.

Carpino, N., Thierfelder, W.E., Chang, M.S., Saris, C., Turner, S.J., Ziegler, S.F., and Ihle, J.N. (2004). Absence of an essential role for thymic stromal lymphopoietin receptor in murine B-cell development. Mol. Cell. Biol. *24*, 2584–2592.

Chen, Y.E., Fischbach, M.A., and Belkaid, Y. (2018). Skin microbiota-host interactions. Nature *553*, 427–436.

Cheng, L.E., and Locksley, R.M. (2014). Allergic inflammation–innately homeostatic. Cold Spring Harb. Perspect. Biol. *7*, a016352.

Chovatiya, R.J., and Colegio, O.R. (2016). Demodicosis in renal transplant recipients. Am. J. Transplant. *16*, 712–716.

Fallon, P.G., Ballantyne, S.J., Mangan, N.E., Barlow, J.L., Dasvarma, A., Hewett, D.R., McIlgorm, A., Jolin, H.E., and McKenzie, A.N. (2006). Identification of an interleukin (IL)-25-dependent cell population that provides IL-4, IL-5, and IL-13 at the onset of helminth expulsion. J. Exp. Med. *203*, 1105–1116.

Finck, R., Simonds, E.F., Jager, A., Krishnaswamy, S., Sachs, K., Fantl, W., Pe'er, D., Nolan, G.P., and Bendall, S.C. (2013). Normalization of mass cytometry data with bead standards. Cytometry A *83*, 483–494.

Forton, F., and Seys, B. (1993). Density of demodex folliculorum in rosacea: a case-control study using standardized skin-surface biopsy. Br. J. Dermatol. *128*, 650–659.

Gause, W.C., Rothlin, C., and Loke, P. (2020). Heterogeneity in the initiation, development and function of type 2 immunity. Nat. Rev. Immunol. *20*, 603–614.

Ge, Y., Miao, Y., Gur-Cohen, S., Gomez, N., Yang, H., Nikolova, M., Polak, L., Hu, Y., Verma, A., Elemento, O., et al. (2020). The aging skin microenvironment dictates stem cell behavior. Proc. Natl. Acad. Sci. USA *117*, 5339–5350.

Georgala, S., Katoulis, A.C., Kylafis, G.D., Koumantaki-Mathioudaki, E., Georgala, C., and Aroni, K. (2001). Increased density of demodex folliculorum and evidence of delayed hypersensitivity reaction in subjects with papulopustular rosacea. J. Eur. Acad. Dermatol. Venereol. *15*, 441–444.

Gieseck, R.L., 3rd, Wilson, M.S., and Wynn, T.A. (2018). Type 2 immunity in tissue repair and fibrosis. Nat. Rev. Immunol. *18*, 62–76.

Gonzales, K.A.U., Polak, L., Matos, I., Tierney, M.T., Gola, A., Wong, E., Infarinato, N.R., Nikolova, M., Luo, S., Liu, S., et al. (2021). Stem cells expand potency and alter tissue fitness by accumulating diverse epigenetic memories. Science *374*, eabh2444.

Gur-Cohen, S., Yang, H., Baksh, S.C., Miao, Y., Levorse, J., Kataru, R.P., Liu, X., de la Cruz-Racelis, J., Mehrara, B.J., and Fuchs, E. (2019). Stem cell-driven lymphatic remodeling coordinates tissue regeneration. Science *366*, 1218–1225.

Harrison, O.J., Linehan, J.L., Shih, H.Y., Bouladoux, N., Han, S.J., Smelkinson, M., Sen, S.K., Byrd, A.L., Enamorado, M., Yao, C., et al. (2019). Commensal-specific T cell plasticity promotes rapid tissue adaptation to injury. Science *363*, eaat6280.

Heibel, H.D., Hendricks, A.J., Foshee, J.P., and Shi, V.Y. (2021). Rosacea associated with dupilumab therapy. J. Dermatolog. Treat. *32*, 114–116.

Hoshino, K., Kashiwamura, S., Kuribayashi, K., Kodama, T., Tsujimura, T., Nakanishi, K., Matsuyama, T., Takeda, K., and Akira, S. (1999). The absence of interleukin 1 receptor-related T1/ST2 does not affect T helper cell type 2 development and its effector function. J. Exp. Med. *190*, 1541–1548.

Howitt, M.R., Lavoie, S., Michaud, M., Blum, A.M., Tran, S.V., Weinstock, J.V., Gallini, C.A., Redding, K., Margolskee, R.F., Osborne, L.C., et al. (2016). Tuft cells, taste-chemosensory cells, orchestrate parasite type 2 immunity in the gut. Science *351*, 1329–1333.

Hu, L., Zhao, Y., Niu, D., Gong, X., and Yang, R. (2019). De novo transcriptome sequencing and differential gene expression analysis of two parasitic human demodex species. Parasitol. Res. *118*, 3223–3235.

Huang, Y., Mao, K., Chen, X., Sun, M.A., Kawabe, T., Li, W., Usher, N., Zhu, J., Urban, J.F., Jr., Paul, W.E., and Germain, R.N. (2018). S1P-dependent interorgan trafficking of group 2 innate lymphoid cells supports host defense. Science *359*, 114–119.

Joost, S., Annusver, K., Jacob, T., Sun, X., Dalessandri, T., Sivan, U., Sequeira, I., Sandberg, R., and Kasper, M. (2020). The molecular anatomy of mouse skin during hair growth and rest. Cell Stem Cell *26*, 441–457.e7.

Katoh, K., and Standley, D.M. (2013). MAFFT multiple sequence alignment software version 7: improvements in performance and usability. Mol. Biol. Evol. *30*, 772–780.

Kleppe, M., Spitzer, M.H., Li, S., Hill, C.E., Dong, L., Papalexi, E., De Groote, S., Bowman, R.L., Keller, M., Koppikar, P., et al. (2017). Jak1 integrates cytokine sensing to regulate hematopoietic stem cell function and stress hematopoiesis. Cell Stem Cell *21*, 489–501.e7.

Kobayashi, T., Voisin, B., Kim, D.Y., Kennedy, E.A., Jo, J.H., Shih, H.Y., Truong, A., Doebel, T., Sakamoto, K., Cui, C.Y., et al. (2019). Homeostatic control of sebaceous glands by innate lymphoid cells regulates commensal bacteria equilibrium. Cell *176*, 982–997.e16.

Lacey, N., Ní Raghallaigh, S., and Powell, F.C. (2011). Demodex mites–commensals, parasites or mutualistic organisms? Dermatology *222*, 128–130.

Lay, K., Yuan, S., Gur-Cohen, S., Miao, Y., Han, T., Naik, S., Pasolli, H.A., Larsen, S.B., and Fuchs, E. (2018). Stem cells repurpose proliferation to contain a breach in their niche barrier. eLife *7*, e41661.

Liang, H.-E., Reinhardt, R.L., Bando, J.K., Sullivan, B.M., Ho, I.C., and Locksley, R.M. (2011). Divergent expression patterns of IL-4 and IL-13 define unique functions in allergic immunity. Nat. Immunol. *13*, 58–66.

Lozupone, C., and Knight, R. (2005). UniFrac: a new phylogenetic method for comparing microbial communities. Appl. Environ. Microbiol. *71*, 8228–8235.

Lozupone, C.A., Hamady, M., Kelley, S.T., and Knight, R. (2007). Quantitative and qualitative beta diversity measures lead to different insights into factors that structure microbial communities. Appl. Environ. Microbiol. *73*, 1576–1585.

Mathur, A.N., Zirak, B., Boothby, I.C., Tan, M., Cohen, J.N., Mauro, T.M., Mehta, P., Lowe, M.M., Abbas, A.K., Ali, N., and Rosenblum, M.D. (2019). Treg-cell control of a CXCL5-IL-17 inflammatory axis promotes hair-follicle-stem-cell differentiation During skin-barrier repair. Immunity *50*, 655–667.e4.

Mayer, J.U., Hilligan, K.L., Chandler, J.S., Eccles, D.A., Old, S.I., Domingues, R.G., Yang, J., Webb, G.R., Munoz-Erazo, L., Hyde, E.J., et al. (2021). Homeostatic IL-13 in healthy skin directs dendritic cell differentiation to promote TH2 and inhibit TH17 cell polarization. Nat. Immunol. *22*, 1538–1550.

McDonald, D., Price, M.N., Goodrich, J., Nawrocki, E.P., DeSantis, T.Z., Probst, A., Andersen, G.L., Knight, R., and Hugenholtz, P. (2012). An improved Greengenes taxonomy with explicit ranks for ecological and evolutionary analyses of bacteria and archaea. ISME J. *6*, 610–618.

Medzhitov, R. (2021). The spectrum of inflammatory responses. Science *374*, 1070–1075.

Mohrs, M., Shinkai, K., Mohrs, K., and Locksley, R.M. (2001). Analysis of type 2 immunity in vivo with a bicistronic IL-4 reporter. Immunity *15*, 303–311.

Nagao, K., Kobayashi, T., Moro, K., Ohyama, M., Adachi, T., Kitashima, D.Y., Ueha, S., Horiuchi, K., Tanizaki, H., Kabashima, K., et al. (2012). Stress-induced production of chemokines by hair follicles regulates the trafficking of dendritic cells in skin. Nat. Immunol. *13*, 744–752.

Naik, S., Larsen, S.B., Cowley, C.J., and Fuchs, E. (2018). Two to tango: dialog between immunity and stem cells in health and disease. Cell *175*, 908–920.

Nashat, M.A., Ricart Arbona, R.J., Lepherd, M.L., Santagostino, S.F., Livingston, R.S., Riedel, E.R., and Lipman, N.S. (2018). Ivermectin-compounded Feed Compared with Topical moxidectin-Imidacloprid for Eradication of demodex musculi in Laboratory Mice. J. Am. Assoc. Lab. Anim. Sci. *57*, 483–497.

Nussbaum, J.C., Van Dyken, S.J., von Moltke, J., Cheng, L.E., Mohapatra, A., Molofsky, A.B., Thornton, E.E., Krummel, M.F., Chawla, A., Liang, H.-E., and Locksley, R.M. (2013). Type 2 innate lymphoid cells control eosinophil homeostasis. Nature *502*, 245–248.

Palopoli, M.F., Fergus, D.J., Minot, S., Pei, D.T., Simison, W.B., Fernandez-Silva, I., Thoemmes, M.S., Dunn, R.R., and Trautwein, M. (2015). Global divergence of the human follicle mite demodex folliculorum: persistent associations between host ancestry and mite lineages. Proc. Natl. Acad. Sci. USA *112*, 15958–15963.

Paus, R., Müller-Röver, S., Van Der Veen, C., Maurer, M., Eichmüller, S., Ling, G., Hofmann, U., Foitzik, K., Mecklenburg, L., and Handjiski, B. (1999). A comprehensive guide for the recognition and classification of distinct stages of hair follicle morphogenesis. J. Invest. Dermatol. *113*, 523–532.

Quint, T., Brunner, P.M., Sinz, C., Steiner, I., Ristl, R., Vigl, K., Kimeswenger, S., Neubauer, K., Pirkhammer, D., Zikeli, M., et al. (2020). Dupilumab for the treatment of atopic dermatitis in an Austrian cohort-real-life data shows rosacea-like folliculitis. J. Clin. Med. *9*, 1241.

Rather, P.A., and Hassan, I. (2014). Human demodex mite: the versatile mite of dermatological importance. Indian J. Dermatol. *59*, 60–66.

Reynolds, G., Vegh, P., Fletcher, J., Poyner, E.F.M., Stephenson, E., Goh, I., Botting, R.A., Huang, N., Olabi, B., Dubois, A., et al. (2021). Developmental cell programs are co-opted in inflammatory skin disease. Science *371*, eaba6500.

Ricardo-Gonzalez, R.R., Schneider, C., Liao, C., Lee, J., Liang, H.E., and Locksley, R.M. (2020). Tissue-specific pathways extrude activated ILC2s to disseminate type 2 immunity. J. Exp. Med. *217*, e20191172.

Ricardo-Gonzalez, R.R., Van Dyken, S.J., Schneider, C., Lee, J., Nussbaum, J.C., Liang, H.E., Vaka, D., Eckalbar, W.L., Molofsky, A.B., Erle, D.J., and Locksley, R.M. (2018). Tissue signals imprint ILC2 identity with anticipatory function. Nat. Immunol. *19*, 1093–1099.

Rosshart, S.P., Herz, J., Vassallo, B.G., Hunter, A., Wall, M.K., Badger, J.H., McCulloch, J.A., Anastasakis, D.G., Sarshad, A.A., Leonardi, I., et al. (2019). Laboratory mice born to wild mice have natural microbiota and model human immune responses. Science *365*, eaaw4361.

Sakamoto, K., Jin, S.P., Goel, S., Jo, J.H., Voisin, B., Kim, D., Nadella, V., Liang, H., Kobayashi, T., Huang, X., et al. (2021). Disruption of the endopeptidase ADAM10-Notch signaling axis leads to skin dysbiosis and innate lymphoid cell-mediated hair follicle destruction. Immunity *54*, 2321–2337.e10.

Sanman, L.E., Chen, I.W., Bieber, J.M., Steri, V., Trentesaux, C., Hann, B., Klein, O.D., Wu, L.F., and Altschuler, S.J. (2021). Transit-amplifying cells coordinate changes in intestinal epithelial cell-type composition. Dev. Cell *56*, 356–365.e9.

Sastre, N., Francino, O., Curti, J.N., Armenta, T.C., Fraser, D.L., Kelly, R.M., Hunt, E., Silbermayr, K., Zewe, C., Sánchez, A., and Ferrer, L. (2016). Detection, prevalence and phylogenetic relationships of demodex spp and further skin prostigmata mites (Acari, Arachnida) in wild and domestic mammals. PLoS One *11*, e0165765.

Schneider, C., Lee, J., Koga, S., Ricardo-Gonzalez, R.R., Nussbaum, J.C., Smith, L.K., Villeda, S.A., Liang, H.E., and Locksley, R.M. (2019). Tissue-resident Group 2 innate lymphoid cells differentiate by layered ontogeny and in situ perinatal priming. Immunity *50*, 1425–1438.e5.

Schneider, C., O'Leary, C.E., von Moltke, J.v., Liang, H.-E., Ang, Q.Y., Turnbaugh, P.J., Radhakrishnan, S., Pellizzon, M., Ma, A., and Locksley, R.M. (2018). A metabolite-triggered tuft cell-ILC2 circuit drives small intestinal remodeling. Cell *174*, 271–284.e14.

Simpson, E.L., Bieber, T., Guttman-Yassky, E., Beck, L.A., Blauvelt, A., Cork, M.J., Silverberg, J.I., Deleuran, M., Kataoka, Y., Lacour, J.P., et al. (2016). Two phase 3 trials of dupilumab versus Placebo in Atopic Dermatitis. N. Engl. J. Med. *375*, 2335–2348.

Smith, G., Manzano Marín, A., Reyes-Prieto, M., Ribeiro Antunes, C.S., Ashworth, V., Goselle, O.N., Jan, A.A.A., Moya, A., Latorre, A., Perotti, M.A., and Braig, H.R. (2022). Human follicular mites: ectoparasites becoming symbionts. Mol. Biol. Evol. *39*, msac125.

Smith, P.C., Zeiss, C.J., Beck, A.P., and Scholz, J.A. (2016). Demodex musculi Infestation in Genetically Immunomodulated Mice. Comp. Med. *66*, 278–285.

Spitzer, M.H., Carmi, Y., Reticker-Flynn, N.E., Kwek, S.S., Madhireddy, D., Martins, M.M., Gherardini, P.F., Prestwood, T.R., Chabon, J., Bendall, S.C., et al. (2017). Systemic immunity is required for effective cancer immunotherapy. Cell *168*, 487–502.e15.

Spitzer, M.H., Gherardini, P.F., Fragiadakis, G.K., Bhattacharya, N., Yuan, R.T., Hotson, A.N., Finck, R., Carmi, Y., Zunder, E.R., Fantl, W.J., et al. (2015). Immunology. An interactive reference framework for modeling a dynamic immune system. Science *349*, 1259425.

Thoemmes, M.S., Fergus, D.J., Urban, J., Trautwein, M., and Dunn, R.R. (2014). Ubiquity and diversity of human-associated demodex mites. PLoS One *9*, e106265.

Van Dyken, S.J., Liang, H.E., Naikawadi, R.P., Woodruff, P.G., Wolters, P.J., Erle, D.J., and Locksley, R.M. (2017). Spontaneous chitin accumulation in airways and age-related fibrotic lung disease. Cell *169*, 497–509.e13.

Van Dyken, S.J., Nussbaum, J.C., Lee, J., Molofsky, A.B., Liang, H.E., Pollack, J.L., Gate, R.E., Haliburton, G.E., Ye, C.J., Marson, A., et al. (2016). A tissue checkpoint regulates type 2 immunity. Nat. Immunol. *17*, 1381–1387.

von Moltke, J., Ji, M., Liang, H.E., and Locksley, R.M. (2016). Tuft-cell-derived IL-25 regulates an intestinal ILC2-epithelial response circuit. Nature *529*, 221–225.

Wang, A., Fogel, A.L., Murphy, M.J., Panse, G., McGeary, M.K., McNiff, J.M., Bosenberg, M., Vesely, M.D., Cohen, J.M., Ko, C.J., et al. (2021). Cytokine RNA in situ hybridization permits individualized molecular phenotyping in biopsies of psoriasis and atopic dermatitis. JID Innov. *1*, 100021.

Yang, H., Adam, R.C., Ge, Y., Hua, Z.L., and Fuchs, E. (2017). Epithelial-mesenchymal micro-niches govern stem cell lineage choices. Cell *169*, 483–496.e13.

Yu, G., Wang, L.G., Han, Y., and He, Q.Y. (2012). clusterProfiler: an R package for comparing biological themes among gene clusters. Omics *16*, 284–287.

Zhao, Y.E., Wang, Z.H., Xu, Y., Xu, J.R., Liu, W.Y., Wei, M., and Wang, C.Y. (2012). Cloning and sequence analysis of chitin synthase gene fragments of demodex mites. J. Zhejiang Univ. Sci. B *13*, 763–768.

Zhao, Y.E., Wu, L.P., Peng, Y., and Cheng, H. (2010). Retrospective analysis of the association between demodex infestation and rosacea. Arch. Dermatol. *146*, 896–902.

Zunder, E.R., Lujan, E., Goltsev, Y., Wernig, M., and Nolan, G.P. (2015). A continuous molecular roadmap to iPSC reprogramming through progression analysis of single-cell mass cytometry. Cell Stem Cell *16*, 323–337.

STAR★METHODS

KEY RESOURCES TABLE

REAGENT or RESOURCE	SOURCE	IDENTIFIER
Antibodies		
Brilliant Violet 421™ anti-mouse CD19 Antibody, 50 μg	BioLegend	Cat#115549; RRID:AB_2563066
Brilliant Violet 421™ anti-mouse TER-119/Erythroid Cells Antibody, 50 μg	BioLegend	Cat#116234; RRID:AB_2562917
Brilliant Violet 421™ anti-mouse Ly-6G/Ly-6C (Gr-1) Antibody, 50 μg	BioLegend	Cat#108445; RRID:AB_2562903
Brilliant Violet 421™ anti-mouse/human CD11b Antibody, 500ul	BioLegend	Cat#101236; RRID:AB_11203704
Brilliant Violet 650™ anti-mouse/human CD11b Antibody	BioLegend	Cat#101259; RRID:AB_2566568
Pacific Blue™ anti-mouse CD11c Antibody, 100 μg	BioLegend	Cat#117322; RRID:AB_755988
Pacific Blue™ anti-mouse CD49b (pan-NK cells) Antibody, 100 μg	BioLegend	Cat#108918; RRID:AB_2249376
Brilliant Violet 421™ anti-mouse CD335 (NKp46) Antibody, 50 μg	BioLegend	Cat#137612; RRID:AB_10915472
Brilliant Violet 421™ anti-mouse NK-1.1 Antibody, 50 μg	BioLegend	Cat#108741; RRID:AB_2562561
BrilliantViolet 421™ anti-mouse TCR γ/δ Antibody, 50 μg	BioLegend	Cat#118120; RRID:AB_2562566)
Pacific Blue™ anti-mouse FcεRIα Antibody, 100 μg	BioLegend	Cat#134314; RRID:AB_10613298
PE/Cy7 anti-mouse CD3 Antibody, 100 μg	BioLegend	Cat#100220; RRID:AB_1732057
Pacific Blue™ anti-mouse F4/80 Antibody, 100 μg	BioLegend	Cat#123124; RRID:AB_893475
Brilliant Violet 711™ anti-mouse CD45 Antibody, 50 μg	BioLegend	Cat#103147; RRID:AB_2564383
BUV395 Rat Anti-Mouse CD45, 50 μg	BD Biosciences	Cat#564279; RRID:AB_2651134
APC/Cyanine7 anti-mouse CD45 Antibody, 100 μg	BioLegend	Cat#103116; RRID:AB_312981
Brilliant Violet 785™ anti-mouse CD90.2 Antibody, 50 μg	BioLegend	Cat#105331; RRID:AB_2562900
Brilliant Violet 605™ anti-mouse CD90.2 Antibody	BioLegend	Cat#105343; RRID:AB_2632889
Brilliant Violet 711™ anti-mouse CD4 Antibody, 500 μl	BioLegend	Cat#100550; RRID:AB_2562099
Pacific Blue™ anti-mouse CD8a Antibody, 100 μg	BioLegend	Cat#100725; RRID:AB_493425
Brilliant Violet 785™ anti-mouse CD8a Antibody	BioLegend	Cat#100750; RRID:AB_2562610
Pacific Blue™ anti-mouse CD5 Antibody	BioLegend	Cat#100642; RRID:AB_2813916
Brilliant Violet 605™ anti-mouse Ly-6A/E (Sca-1) Antibody, 125 μL	BioLegend	Cat#108133; RRID:AB_2562275
Brilliant Violet 711™ anti-mouse I-A/I-E Antibody	BioLegend	Cat#107643; RRID:AB_2565976
PerCP/Cyanine5.5 anti-mouse CD326 (Ep-CAM) Antibody	BioLegend	Cat#118220; RRID:AB_2246499
FITC anti-human/mouse CD49f Antibody	BioLegend	Cat#313606; RRID:AB_345300
PE/Cyanine7 anti-human/mouse CD49f Antibody	BioLegend	Cat#313622; RRID:AB_2561705
Alexa Fluor® 647 Rat anti-Mouse CD34	BD Biosciences	Cat#560230; RRID:AB_1645200
CD127 (IL-7R) Monoclonal Antibody (A7R34), APC-eFluor 780	Invitrogen	Cat#47-1271-82; RRID:AB_1724012
Gata-3 Monoclonal Antibody (TWAJ), eFluor 660, eBioscience™, 100 tests	Invitrogen	Cat#50-9966-42; RRID:AB_10596663
APC anti-human CD4 Antibody	BioLegend	Cat#300514; RRID:AB_314082
FOXP3 Monoclonal Antibody (FJK-16s), eBioscience™	Invitrogen	Cat#11-5773-82; RRID:AB_465243
BV605 Rat Anti-Mouse IL-33R (ST2), 50 μg	BD Biosciences	Cat#745257; RRID:AB_2742841
CD218a (IL-18Ra) Monoclonal Antibody (P3TUNYA), PerCP-eFluor 710, eBioscience™, 100 μg	Invitrogen	Cat#46-5183-82; RRID:AB_2573764
Living Colors® DsRedPolyclonal Antibody (100μl)	TakaraBio	Cat#632496; RRID:AB_10013483
Ki-67 Monoclonal Antibody (SolA15), FITC, eBioscience™	Invitrogen	Cat#11-5698-82; RRID:AB_11151330
FITC Mouse Anti-E-Cadherin	BD Biosciences	Cat#612131; RRID:AB_2076677
Goat anti-Rabbit IgG (H+L) Cross-Adsorbed Secondary Antibody, Alexa Fluor 555	Invitrogen	Cat#A-21428; RRID:AB_2535849
Anti-human CD3e	Cell Signaling Technology	Cat#85061; RRID:AB_2721019

(*Continued on next page*)

Continued

REAGENT or RESOURCE	SOURCE	IDENTIFIER
Purified anti-mouse TER-119/Erythroid Cells (Maxpar® Ready) Antibody	BioLegend	Cat#116241; RRID:AB_2563789
Purified anti-mouse CD45 (Maxpar® Ready) Antibody	BioLegend	Cat#103141; RRID:AB_2562800
BD Transduction Laboratories™ Purified Mouse Anti-Stat3 (pS727)	BD Biosciences	Cat#612542; RRID:AB_399839
Purified anti-mouse CD326 (Ep-CAM) (Maxpar® Ready) Antibody	BioLegend	Cat#118223; RRID:AB_2563743
Purified anti-mouse/human CD11b (Maxpar® Ready) Antibody	BioLegend	Cat#101249; RRID:AB_2562797
Anti-Histone H3 (phospho S28) antibody [HTA28]	Abcam	Cat#ab10543; RRID:AB_2295065
BD Pharmingen™ Purified Hamster Anti-Mouse CD11c	BD Biosciences	Cat#553799; RRID:AB_395058
Phospho-MAPKAPK-2 (Thr334) (27B7)	Cell Signaling Technology	Cat#3007; RRID:AB_490936
Phospho-CREB (Ser133) (87G3) Rabbit mAb	Cell Signaling Technology	Cat#9198; RRID:AB_2561044
BD Transduction Laboratories™ Purified Mouse Anti-Stat1 (pY701)	BD Biosciences	Cat#612232; RRID:AB_399555
BD Transduction Laboratories™ Purified Mouse Anti-Human Stat5 (pY694)	BD Biosciences	Cat#611964; RRID:AB_399385
Phospho-S6 Ribosomal Protein (Ser235/236) (2F9) Rabbit mAb	Cell Signaling Technology	Cat#4856; RRID:AB_2181037
Purified anti-mouse Ly-6C (Maxpar® Ready) Antibody	BioLegend	Cat#128039; RRID:AB_2563783
Phospho-p44/42 MAPK (Erk1/2) (Thr202/Tyr204) (D13.14.4E) XP® Rabbit mAb	Cell Signaling Technology	Cat#4370; RRID:AB_2315112
Anti-Human CyclinB1 (GNS-1)-153Eu	Fluidigm	Cat#3153009A
BD Transduction Laboratories™ Purified Mouse Anti-p38 MAPK (pT180/pY182)	BD Biosciences	Cat#612288; RRID:AB_399605
Purified anti-mouse CD8a (Maxpar® Ready) Antibody	BioLegend	Cat#100755; RRID:AB_2562796
Purified anti-mouse CD4 (Maxpar® Ready) Antibody	BioLegend	Cat#100561; RRID:AB_2562762
BD Pharmingen™ Purified Rat Anti-Mouse CD3 Molecular Complex	BD Biosciences	Cat#555273; RRID:AB_395697
Purified anti-mouse Ly-6G (Maxpar® Ready) Antibody	BioLegend	Cat#127637; RRID:AB_2563784
Phospho-4E-BP1 (Thr37/46) (236B4) Rabbit mAb	Cell Signaling Technology	Cat#2855; RRID:AB_560835
BD Transduction Laboratories™ Purified Mouse Anti-Human ZAP-70 (pY319)/Syk (pY352)	BD Biosciences	Cat#612574; RRID:AB_399863
Phospho-TBK1/NAK (Ser172) (D52C2) XP® Rabbit mAb	Cell Signaling Technology	Cat#5483; RRID:AB_10693472
Purified anti-mouse TCR γ/δ Antibody	BioLegend	Cat#118101; RRID:AB_313826
IκBα (L35A5) Mouse mAb (Amino-terminal Antigen)	Cell Signaling Technology	Cat#4814; RRID:AB_390781
alpha-Fetoprotein/AFP Antibody (SPM334)	Novus	Cat#NBP2-32915
BD Transduction Laboratories™ Purified Mouse Anti-Stat 6 (pY641)	BD Biosciences	Cat#611566; RRID:AB_399012
Anti-pRb [S807/S811] (J112-906)-166Er	Fluidigm	Cat#3166011A
FOXP3 Monoclonal Antibody (NRRF-30)	eBioscience	Cat#14-4771-80; RRID:AB_529583
Purified anti-mouse NK-1.1 (Maxpar® Ready) Antibody	BioLegend	Cat#108743; RRID:AB_2562803
Ki-67 Monoclonal Antibody (SolA15)	eBioscience	Cat#14-5698-82; RRID:AB_10854564
BD Transduction Laboratories™ Purified Mouse Anti-Stat4	BD Biosciences	Cat#610926; RRID:AB_398241
Purified anti-mouse CD62L (Maxpar® Ready) Antibody	BioLegend	Cat#104443; RRID:AB_2562802
BD Pharmingen™ Purified Rat Anti-Mouse Siglec-F	BD Biosciences	Cat#552125; RRID:AB_394340
Purified anti-mouse CD19 (Maxpar® Ready) Antibody	BioLegend	Cat#115547; RRID:AB_2562806
BD Pharmingen™ Purified Rat Anti-Mouse CD34	BD Biosciences	Cat#553731; RRID:AB_395015
BD Pharmingen™ Purified Rat Anti-Mouse CD44	BD Biosciences	Cat#553131; RRID:AB_394646
Purified anti-mouse I-A/I-E (Maxpar® Ready) Antibody	BioLegend	Cat#107637; RRID:AB_2563771
Chemicals, peptides, and recombinant proteins		
Recombinant mouse IL-4	R&D systems	Cat#404-ML-050/CF
Recombinant mouse IL-13	R&D systems	Cat#413-ML-050/CF

(*Continued on next page*)

Continued

REAGENT or RESOURCE	SOURCE	IDENTIFIER
Recombinant mouse IL-13	BioLegend	Cat#575908
Recombinant mouse IL-7	BioLegend	Cat#577804
Recombinant mouse TSLP	R&D systems	Cat#555-TS-010/CF
Recombinant mouse IL-18	BioLegend	Cat#767004
Recombinant mouse IL-33	BioLegend	Cat#580504
Cell Activation Cocktail (without Brefeldin A)	BioLegend	Cat#423301
InVivoMAb anti-mouse CD16/CD32, Clone 2.4G2	BioXCell	Cat#BE0307
InVivoMAb anti-mouse IL-4, clone 11B11	BioXCell	Cat#BE0045
TrueStain FcX (anti-mouse CD16/32 antibody (clone 93)	BioLegend	Cat#101320
Moxidectin	Sigma-Aldrich	Cat#33746-25MG
Imidacloprid	Sigma-Aldrich	Cat#37894-100MG
Ampicillin	Sigma-Aldrich	Cat#A1593-25G
Kanamycin	Sigma-Aldrich	Cat#K1637-25G
Neomycin	Sigma-Aldrich	Cat#N1876-100G
Vancomycin	Sigma-Aldrich	Cat#V2002-5G
Metronidazole	Sigma-Aldrich	Cat#M1547-25G
5-Ethynyl-2′-deoxyuridine (EdU)	Sigma-Aldrich	Cat#900584
Nair depilatory cream	Nivea	N/A
RPMI-1640 Medium	Sigma-Aldrich	Cat#R8758
Liberase TL	Sigma-Aldrich	Cat#5401020001
DNAse I	Sigma-Aldrich	Cat#10104159001
Fetal Bovine Serum	Sigma-Aldrich	Cat#F0926-500ML
4',6-Diamidine-2′-phenylindole dihydrochloride (DAPI)	Roche	Cat#10236276001
Live/Dead fixable dye	Thermofisher	Cat#L34968
Trypsin-EDTA	ThermoFisher	Cat#15400-054
HEPES	Sigma-Aldrich	Cat#H3537-100ML
Penicillin/Streptomycin	Fisher	Cat#15140122
5-Iodo-2′-deoxyuridine (IdU)	Sigma-Aldrich	Cat#I7125
Cisplatin	Sigma-Aldrich	Cat#P4394-25MG
Paraformaldehyde	Fisher	Cat#15713
Bovine Serum Albumin (BSA)	Sigma-Aldrich	Cat#A7906-500G
Goat Serum	Sigma-Aldrich	Cat#G9023-10ML
Blocking Reagent	Perkin Elmer	Cat#FP1012
Mounting Media	Vector Laboratories	Cat#H-1000
ProLong Gold Antifade	ThermoFisher	Cat#P36930
1x DPBS	Life Technologies	Cat#14190-250
191/193Ir DNA inercalator	Fluidigm	Cat#201192B
Q5 High-Fidelity DNA Polymerase	NEB	M0494L
Yeast cell lysis buffer	Lucigen	Cat#MPY80200
Lucifer yellow	ThermoFisher	Cat#L453
Optimal Cutting Temperature Compound O.C.T.	VWR	Cat#25608-930
Tris-HCl (1M)	Fisher	Cat#50843267
NaCl (5M)	Fisher	Cat#AM9760G
Proteinase K	Thomas Scientific	Cat#C755H28
Citrate buffer (pH 6.0)	ThermoFisher	Cat#00500
3% hydrogen peroxide	JT Baker	Cat#JT-2186-01
ImmPRESS horseradish peroxidase reagent	Vector Laboratories	Cat#MP-7451
Diaminobenzidine substrate	Vector Laboratories	Cat#SK-4100

(*Continued on next page*)

Continued

REAGENT or RESOURCE	SOURCE	IDENTIFIER
Commercial Assays		
CountBright Absolute Counting Beads	Life Technologies	Cat#C36950
Click-IT Plus EdU imaging kit	ThermoFisher	Cat#C10637
Click-IT Plus EdU flow cytometry kit	ThermoFisher	Cat#C10633
MaxPAR antibody conjugation kit	Fluidigm	Cat#201300
DNEasy PowerSoil Pro Kit	Qiagen	Cat#47014
Chromium Single Cell 3' GEM, Library & Gel Bead Kit v3.1	10X Genomics	Cat#PN-1000121
Cytokine Bead Array Flex Sets: IL-4	BD Biosciences	Cat#558298
Cytokine Bead Array Flex Sets: IL-5	BD Biosciences	Cat#558302
Cytokine Bead Array Flex Sets: IL-13	BD Biosciences	Cat#558349
Cytokine Bead Array Flex Sets: IL-17A	BD Biosciences	Cat#560283
LEGEND MAXTMMouse IL-22 ELISA Kit	BioLegend	Cat#436307
RNeasy Micro Plus kit	Qiagen	Cat#74034
SuperScript VILO cDNA synthesis kit	ThermoFisher	Cat#11754250
Power SYBR Green PCR master mix	ThermoFisher	Cat#4368702
RNAscope® 2.5 HD Reagent Kit-RED	ACD Bio/Bio-Techne	Cat#322350
RNAscope® Probe- Hs-*IL4*	ACD Bio/Bio-Techne	Cat#315191
RNAscope® Probe- Hs-*IL5*	ACD Bio/Bio-Techne	Cat#319391
RNAscope® Probe- Hs-*IL13*	ACD Bio/Bio-Techne	Cat#586241
RNAscope® Probe- Hs-*IL22*	ACD Bio/Bio-Techne	Cat#560811
RNAscope® Probe- Hs-*IFNG*	ACD Bio/Bio-Techne	Cat#310501
Deposited data		
Single cell RNA-sequencing data	This paper	GEO: GSE197983
16S rRNA sequencing data	This paper	BioProject: PRJNA861245
Experimental models: Organisms/strains		
Mouse: Wild type: C57BL/6J	The Jackson Laboratory	Stock# 000664
Mouse: Red5: B6(C)-*Il5*$^{tm1.1(icre)Lky}$/J	The Jackson Laboratory	Stock# 030926
Mouse: Yarg: B6.129S4-*Arg1*^{tm1Lky}/J	The Jackson Laboratory	Stock# 015857
Mouse: Smart13: B6.129S4(C)-*Il13*$^{tm2.1Lky}$/J	The Jackson Laboratory	Stock# 031367
Mouse: B6.129S2(C)-Stat6^{tm1Gru}/J	The Jackson Laboratory	Stock# 005977
Mouse: B6.*Il4ra*−/−: BALB/c-*Il4ra*^{tm1Sz}/J	The Jackson Laboratory	Stock# 003514
Mouse: B6.*Il4/Il13*−/−	Liang et al., 2012	N/A
Mouse: B6.*Il4*–/–: Il4t$^{m1(CD2)Mmrs}$(KN2/KN2)	Mohrs et al., 2001	N/A
Mouse: B6.129S7-Rag1^{tm1Mom}/J	The Jackson Laboratory	Stock# 002216
Mouse: B6.129S6-*Rag2*^{tm1Fwa} N12: ko/ko	Taconic Biosciences	Cat# RAGN12-F
Mouse: C57BL/6NTac.Cg-*Rag2*^{tm1Fwa} *Il2rg*^{tm1Wjl}: ko/ko;ko/ko (*Rag2*–/–/*Il2rg*–/–)	Taconic Biosciences	Cat# 4111-F
Mouse: B6.*Crlf2*−/−	Carpino et al., 2004	N/A
Mouse: B6.*Il1rl1*−/−	Hoshino et al., 1999	N/A
Mouse: B6.*Il25*−/−: B6.*Il25*^{tm1Anjm}	Fallon et al., 2006	N/A
Mouse: B6.*Il18*–/–:B6.129P2-*Il18*^{tm1Aki}/J	The Jackson Laboratory	Stock# 004130
Mouse: B6.*Il13ra1*–/–	This paper	N/A
Oligonucleotides		
qPCR Primer: *Il13*-forward: 5'-CCTGGCTCTTGCTTGCCTT-3'	PrimerBank	PrimerBank ID:6680403a1
qPCR Primer: *Il13*-reverse: 5'-GGTCTTGTGTGATGTTGCTCA-3'	PrimerBank	PrimerBank ID:6680403a1
qPCR Primer: *Il22*-forward 5'- ATGAGTTTTTCCCTTATGGGGAC-3'	PrimerBank	PrimerBank ID:21426819a1

(*Continued on next page*)

Continued

REAGENT or RESOURCE	SOURCE	IDENTIFIER
qPCR Primer: *Il22*-reverse 5'- GCTGGAAGTTGGACACCTCAA-3'	PrimerBank	PrimerBank ID:21426819a1
qPCR Primer: *Cdkn2a/p16*-forward: 5'-CGCAGGTTCTTGGTCACTGT-3'	PrimerBank	PrimerBank ID:6753390a1
qPCR Primer: *Cdkn2a/p16*-reverse: 5'-TGTTCACGAAAGCCAGAGCG-3'	PrimerBank	PrimerBank ID:6753390a1
qPCR Primer: *Rps17*-forward: 5'-CCAAGACCGTGAAGAAGGCTG-3'	PrimerBank	PrimerBank ID:6677801a1
qPCR Primer: *Rps17*-reverse: 5'-GCTGGGGATAATGGCGATCT-3'	PrimerBank	PrimerBank ID:6677801a1
Primer: CHS-forward: 5'-GAAGCGGCGAGTAATGTTCATC-3'	This paper	N/A
Primer: CHS-reverse: 5'-CCTGACTCCATCTTTTACGATGTC-3'	This paper	N/A
Primer: Keratin 5-forward: 5'-TCTGCCATCACCCCATCTGT-3'	PrimerBank	PrimerBank ID:20911031a1
Primer: Keratin 5-reverse: 5'-CCTCCGCCAGAACTGTAGGA-3'	PrimerBank	PrimerBank ID:20911031a1
Primer: 18S-forward: 5'-TCCAAGGAAGGCAGCAGGCA-3'	This paper	N/A
Primer: 18S-reverse: 5'-CGCGGTAGTTCGTCTTGCGACG-3'	This paper	N/A
16s rRNA gene forward: 5'-AGAGTTTGATCCTGGCTCAG-3'	This paper	N/A
16s rRNA gene reverse: 5'-ATTACCGCGGCTGCTGG-3'	This paper	N/A
sgRNA targeting exon 2 of *Il13ra1* gene: ACGCTCAAATTCGTCACAGGTGG	This paper	N/A
sgRNA targeting exon 2 of *Il13ra1* gene: TCCTGAGCCACAGCATGTACTGG)	This paper	N/A
Genotyping primer: Il13Ra1-Forward: 5'-AAAGTGAAGCCATCAGTAGTCCCTC-3'	This paper	N/A
Genotyping primer: Il13Ra1-Reverse: 5'-AAATGCAAACCCACCCACCACTAAC-3'	This paper	N/A
Recombinant DNA		
eGFP-CBP plasmid	This study	https://www.addgene.org/169211/
Software and algorithms		
ImageJ Software	https://imagej.net/software/fiji/	N/A
Significance Across Microarrays algorithm	Bair and Tibshirani, 2004; Bruggner et al., 2014	N/A
Scaffold maps R package	https://github.com/spitzerlab/statisticalScaffold	N/A
viSNE and Spade analyses	www.Cytobank.org	N/A
Flow Cytometric Analysis Program (FCAP) Array software	https://www.beckman.com/flow-cytometry/software	N/A
SoftMax Pro software	Molecular Devices	N/A
Flowjo (v10.6.1)	https://www.flowjo.com	N/A
BD FACSDiva Software	BD Biosciences	N/A
GraphPad Prism	https://www.graphpad.com/scientific-software/prism/	N/A
Quantity One (v4.6.1)	Bio-Rad Laboratories	N/A
Image Lab (v6.1.0)	Bio-Rad Laboratories	N/A

(*Continued on next page*)

Continued

REAGENT or RESOURCE	SOURCE	IDENTIFIER
QIIME2	Bolyen et al., 2019	N/A
DADA2	Callahan et al., 2016	N/A
Greengenes Reference Database	McDonald et al., 2012	N/A
MAFFT	Katoh and Standley, 2013	N/A
Principal Coordinates Analysis of weighted and unweighted UniFrac distance	Lozupone and Knight, 2005; Lozupone et al., 2007	N/A
scikit-bio	Bokulich et al., 2018	N/A
Seurat V3 or V4	https://satijalab.org/seurat/	N/A
R package Harmony	https://github.com/immunogenomics/harmony	N/A
Gorilla	http://cbl-gorilla.cs.technion.ac.il	N/A
Nebulosa Package	https://github.com/powellgenomicslab/Nebulosa	N/A
Mass cytometry data normalization algorithm	Finck et al., 2013	N/A
AxioVision Software	Zeiss	N/A
NIS Elements Software	Nikon	N/A

RESOURCE AVAILABILITY

Lead contact

Further information and requests for reagents may be directed to, and will be fulfilled by, the lead contact Richard Locksley (richard.locksley@ucsf.edu).

Materials availability

All reagents generated or used in this study are available on request from the lead contact with a completed Materials Transfer Agreement. Information on reagents used in this study is available in the key resources table.

Data and code availability

All the data supporting the findings of the article are available within the main text or supplemental information. The published article includes datasets generated during this study. Original single cell RNA-seq data has been deposited in GEO: GSE197983. Original 16S rRNA sequencing datasets analyzed in this study are available at the NCBI BioProject: PRJNA861245.

METHOD DETAILS

Mice

Wild-type (C57BL/6J; Stock 000664) mice were purchased from Jackson Laboratories. *Il5*^{Red5}, *Arg1*^{Yarg}, and *Il13*^{Smart} reporter alleles on C57BL/6J (B6) backgrounds were bred and maintained as described (Bando et al., 2013; Ricardo-Gonzalez et al., 2018). For some experiments, mice encoding the *Arg1*^{Yarg} and/or *Il13*^{Smart} reporter alleles that do not impact the endogenous gene expression were used as wild-type controls. *Il4ra*$^{-/-}$ (BALB/c-Il4ratm1Sz/J; 003514) and Stat6$^{-/-}$ (B6.129S2(C)-Stat6tm1Gru/J; 005977) mice were initially purchased from The Jackson Laboratory and backcrossed to C57BL/6J for at least eight generations as described (von Moltke et al., 2016). Additional wild-type C57BL/6J and *Il4ra*$^{-/-}$ mice on the C57BL/6J background were obtained from the UCSF colony of M.S. Fassett and K.M. Ansel. *Il4*$^{-/-}$*Il13*$^{-/-}$ mice were generated as previously described and backcrossed C57BL/6J for at least eight generations (Liang et al., 2011). *Il4*$^{-/-}$ (KN2/KN2 mice) were generated as previously described (Mohrs et al., 2001) and backcrossed to C57BL/6J. *Crlf2*$^{-/-}$ (Carpino et al., 2004), *Il25*$^{-/-}$ (Fallon et al., 2006), and *Il1rl1*$^{-/-}$ (Hoshino et al., 1999) mice on C57BL/6 J backgrounds were intercrossed to generate *Crlf2*$^{-/-}$,*Il25*$^{-/-}$,*Il1rl1*$^{-/-}$ triple-deficient mice expressing *Il5*^{Red5}, *Arg1*^{Yarg}, and *Il13*^{Smart} reporter alleles as previously described (Ricardo-Gonzalez et al., 2018; Van Dyken et al., 2016). Triple-deficient mice were crossed to Il18$^{-/-}$ mice (Stock 004130) purchased from The Jackson Laboratory to generate *Crlf2*$^{-/-}$,*Il25*$^{-/-}$,*Il1rl1*$^{-/-}$,*Il18*$^{-/-}$ quadruple-ablated (Quad-ablated) in combination with *Il5*^{Red5}, *Arg1*^{Yarg}, and *Il13*^{Smart} reporter alleles. *Rag1*$^{-/-}$ mice (Stock 002216) were purchased from Jackson laboratory, and crossed to *Arg1*^{Yarg} and *Il5*^{Red5} reported alleles. *Rag2*$^{-/-}$ (Stock RAGN12-F) and *Rag2*$^{-/-}$*Il2rg*$^{-/-}$ (Stock 4111-F) mice were obtained from Taconic Biosciences. For all experiments, sex-matched mice aged 7-14 weeks were used unless otherwise indicated. Mice were maintained under specific pathogen-free conditions. For *in vivo* cytokine treatments, mice were injected subcutaneously with IL-4 complex (IL-4c) comprised rmIL-4 (2 μg, R&D systems) combined with anti-IL-4 antibody (10 μg, Clone Mab 11B11, BioXcell), or rmIL-13 (2 μg, R&D systems) in calcium- and magnesium-free phosphate

buffered saline (PBS). For co-housing experiments, mice of the appropriate genotypes were co-housed for 6-12 weeks in the ratios noted in the figure legends. For treatment with topical anti-parasitic agents, a stock solution in 70% ethanol of moxidectin (Sigma 33746) and imidacloprid (Sigma 37894) was prepared and diluted to a working solution of (0.83 mg/ml moxidectin and 3.33 mg/ml imidacloprid) and applied topically to intrascapular skin at 3.3 mg/kg moxidectin and 13.3 mg/kg imidacloprid. Control mice were treated with 70% ethanol. For broad-spectrum antibiotics treatment, mice received drinking water supplemented with ampicillin, kanamycin, and neomycin (all 1 mg/ml), vancomycin (0.5 mg/ml), and metronidazole (2.5 mg/ml) in 1% sucrose. For EdU experiments, mice received a peritoneal injection of 1 μg of EdU (Sigma 900584) 14-18 hours prior to harvesting. All animal procedures were approved by the UCSF Institutional Animal Care and Use Committee.

Generation of IL-13Ra1 deficient mice

Two sgRNAs targeting exon 2 of *Il13ra1* gene (**ACGCTCAAATTCGTCACAGGTGG** and **TCCTGAGCCACAGCATGTACTGG**) and recombinant Cas9 (PNA Bio) were simultaneously injected as RNPs into the zygotes obtained from C57BL/6 J mice carrying *Arg1*$^{Yarg/Yarg}$, *Il5*^{Red5}, and *Il13*^{Smart} reporter alleles. Founders were screened by PCR using primers: Il13Ra1-Forward: 5'-AAAGT GAAGCCATCAGTAGTCCCTC-3' and Il13Ra1-Reverse: 5'-AAATGCAAACCCACCCACCACTAAC-3' to identify a ~144 bp deletion resulted from the end-joining event of two DSBs at the sgRNA-targeted sites. Since the *Il13ra1* gene is an X-linked gene, only positive male founders were chosen to ensure the allelic identity. A male founder was first crossed with C57BL/6 J mice (with *Arg1*$^{Yarg/Yarg}$, *Il5*^{Red5}, and *Il13*^{Smart} reporter alleles) followed by intercrossing to obtain homozygous female *Il13ra1*$^{-/-}$.

Depilation experiment

Mice were anesthetized with isoflurane inhalation. Under anesthesia, the dorsal surface (back) hair of the animals was shaved down to the level of skin with an electric razor. A thin coat (1 fingertip unit) of Nair depilatory cream (Nivea) was applied to the shaved region for a period of 30 s before wiping clean. For monitoring of clinical hair regrowth, standardized pictures were taken with a ruler on the day of depilation (day 0) and then at days 4, 7, 9, 11, 14. Anagen induction was quantified using intensity analysis on ImageJ software (NIH, USA) at each time point or as a percent of pigmented dorsal skin relative to baseline (day 0). For repeat depilation experiments, mice were initially shaved and depilated when they were in second telogen (2 months old). Cycles were repeated once a month once they have completed the anagen and recovery phase. Tissues were analyzed for flow cytometry, stem cell proliferation, and qPCR as described below.

Flow cytometry and cell sorting

Whole skin single cell suspensions were prepared as described previously (Ricardo-Gonzalez et al., 2018). Briefly, back tissue was minced in RPMI-1640 with 5% FBS, then transferred to C tubes (Miltenyi Biotec), containing 5 ml of RPMI-1640 (Sigma R8758) supplemented with Liberase TL (0.25 mg/ml, Sigma 5401020001), and DNAse I (0.1 mg/ml; Sigma 10104159001). Samples were shaken at 250 rpm for 2 hours at 37 °C, then dispersed using an automated tissue dissociator (GentleMACS; Miltenyi Biotec) running program C. Single-cell suspensions were passed through a 70 μm filter and washed twice with RPMI containing 5% FBS. The following antibodies, all from BioLegend (unless otherwise specified, see key resources table and Table S2) were used at 1:300 dilution unless noted: anti-CD3 (17A2, diluted 1:200), anti-CD4 (RM4-5, diluted 1:100), anti-CD5 (53-7.3), anti-CD8α (53-6.7, diluted 1:100), anti-CD11b (M1/70), anti-CD11c (N418), anti-CD19 (6D5), anti-CD25 (PC61, diluted 1:100), anti-CD45 (30F-11, BD Biosciences), anti-CD49b (DX5; eBiosciences), anti-CD127 (A7R34, diluted 1:100), anti-CD218 (P3TUNYA,eBiosciences), anti-F4/80 (BM8), anti-Gr-1 (RB6-8C5), anti-NK1.1 (PK136), anti-NKp46 (29A1.4), anti-Thy1.2 (30-H12; diluted 1:1000); anti-human CD4 (RPA-T4, diluted 1:20; eBiosciences), anti-GATA3 (TWAJ, diluted 1:25), anti-FoxP3 (FJK-16s, Invitrogen, diluted 1:100), anti-T1/ST2 (U29-93; BD Biosciences, diluted 1:200). Live/dead cell exclusion was performed with DAPI (4′,6-diamidine-2′-phenylindole dihydrochloride; Roche) or LIVE/dead fixable dye (Thermofisher). Cell counts were performed using flow cytometry counting beads (CountBright Absolute; Life Technologies) per manufacturer instructions. To assay cell proliferation, the Click-IT EdU flow cytometry or imaging kits (ThermoFisher) were used according to the kit instructions. Sample data were acquired with a 5-laser LSRFortessa X-20 flow cytometer and BD FACSDiva software (BD Biosciences) and analyzed using FlowJo software (Tree Star v10.6.1).

ILC2s were sorted from reporter mice as live (DAPI$^-$), Lin(CD3, CD4, CD8, TCRγδ CD11b, CD11c, CD19, NK1.1, NKp46, Gr-1, F4/80, Ter119, DX5)$^-$CD45$^+$Thy1$^+$Red5$^+$ using a MoFlo XDP (Beckman Coulter). Epithelial cell preparations for flow cytometry or CyTOF analyses were prepared as previously described (Ali et al., 2017; Nagao et al., 2012). Briefly, mice were shaved and dorsal skin was harvested and trimmed of fat. The tissue was floated in 4 ml of 0.25% Trypsin-EDTA (Thermo Fisher) and incubated for 90 min at 37 °C. The epidermis was scrapped from the dermis and mechanically separated by pipetting into complete media (RPMI-1640 supplemented with 10% FBS, HEPES, Penicillin/Streptomycin). The cell suspension was passed through a 100 μm strainer and washed with 10 ml of complete media. The cell suspension was then pelleted, filtered through a 40 μm filter and aliquoted for cell staining. The following antibodies were used for staining epithelial fractions: anti-Sca1 (D7, 1:300); anti-MHCII (M5/114.15.2, 1:400); anti-CD326 (G8.8, 1:300); anti-CD45 (30F-11, 1:400); anti-CD34 (RAM34, 1:200); anti-CD49f (GoH3, 1:300).

Adoptive transfer of ILC2s

For adoptive transfer of ILC2s, *Demodex*-infected *Il4ra*$^{-/-}$ mice were co-housed with *Rag1*$^{-/-}$*Arg1*^{Yarg} *Il5*^{Red5} reporter mice for four weeks to establish *Demodex* infection. ILC2s (LiveCD45$^+$Lin$^-$Thy1$^+$Red5$^+$) from the *Demodex*-infected *Rag1*$^{-/-}$ mice were sorted from skin, lung and fat. Recipient *Rag2*$^{-/-}$*Il2rg*$^{-/-}$ mice received 2.5 x 10^4 pooled ILC2 cells intravenously in 200 μl of PBS at two weeks

before, and 7 x 10^4 pooled ILC2s at the start of co-housing. Control mice received PBS. Mice were co-housed with *Demodex*-infected *Il4ra*$^{-/-}$ for 6 weeks before analysis.

Mass cytometry

Sample preparation

Mass cytometry was performed as described (Kleppe et al., 2017). Briefly, single-cell suspension from the epidermal fraction of the various mice strains were prepared. To test the responsiveness to type 2 immune signaling, mice were treated with s.c. IL-4 complex for 30-60 min prior to harvest. IdU (200 μl of 5mM stock solution, Sigma I7125) was injected 20-30 min prior to harvesting. Cells were incubated with 25 μM Cisplatin for 1 min and fixed with paraformaldehyde at 1.6% for 10 min at room temperature (RT). Cell pellets were stored at –80 °C until analysis. Prior to antibody staining, cells were thawed and mass tag cellular barcoding of prepared samples was performed by incubating cells with distinct combinations of isotopically-purified palladium ions chelated by isothiocyanobenzyl-EDTA in 0.02% saponin in PBS as previously described (Behbehani et al., 2014; Zunder et al., 2015). After two washes with staining media (PBS + 0.5% BSA + 0.02% NaN_3), sets of 20 barcoded samples were pooled together and washed once more with staining media. Antibody staining was performed using a panel of antibodies and metals that were purchased directly conjugated (Fluidigm) or conjugated using 100 μg of antibody lots combined with the MaxPAR antibody conjugation kit (Fluidigm) according to the manufacturer's instructions and detailed in Table S3. Surface marker antibodies were added to a 500 μL final reaction volumes and stained for 30 min at RT on a shaker. Following staining, cells were washed twice with PBS with 0.5% BSA and 0.02% NaN3. Then cells were permeabilized with 4 °C methanol for 10 min at 4 °C followed by two washes in PBS with 0.5% BSA and 0.02% NaN_3 to remove remaining methanol. The intracellular antibodies were added in 500 μL for 30 min at RT on a shaker. Cells were washed twice in PBS with 0.5% BSA and 0.02% NaN_3 and stained with 1 mL of 1:4000 191/193Ir DNA intercalator (Fluidigm) diluted in PBS with 1.6% PFA overnight. Cells were washed once in PBS with 0.5% BSA and 0.02% NaN_3 and twice with double-deionized (dd)H_20. We analyzed 1 x 10^6 cells per animal, per tissue, per condition consistent with generally accepted practices in the field.

Bead standard data normalization

Just before analysis, the stained and intercalated cell pellet was resuspended in ddH_2O containing the bead standard at a concentration ranging between 1 and 2 x 10^4 beads/ml as described (Finck et al., 2013). The bead standards were prepared immediately before analysis, and the mixture of beads and cells was filtered through filter cap FACS tubes (BD Biosciences) before analysis. Mass cytometry files were normalized together using the mass cytometry data normalization algorithm (Finck et al., 2013), which uses the intensity values of a sliding window of these bead standards to correct for instrument fluctuations over time and between samples.

Scaffold map generation

Total live leukocytes (excluding erythrocytes) were used for all analyses. Cells from each tissue for all animals were clustered together (rather than performing CLARA clustering on each file individually as originally implemented in Spitzer et al., 2015) Cells were deconvolved into their respective samples. Cluster frequencies or the Boolean expression of Ki67 for each cluster were passed into the Significance Across Microarrays algorithm (Bair and Tibshirani, 2004; Bruggner et al., 2014), and results were tabulated into the Scaffold map files for visualization through the graphical user interface. Cluster frequencies were calculated as a percent of total live nucleated cells (excluding erythrocytes). Scaffold maps were then generated as previously reported (Spitzer et al., 2017; Spitzer et al., 2015). All analyses were performed using the open source Scaffold maps R package available at http://www.github.com/spitzerlab/statisticalScaffold.

Spade and viSNE generation

viSNE and Spade analyses were performed with Cytobank (www.cytobank.org).

Cytokine quantification

Cytokine in mouse serum or ILC2 culture supernatants were measured according to the manufacturer's protocol using the following Cytokine Bead Array Flex Sets (BD): IL-4 (#558298), IL-5 (#558302), IL-13 (#558349), and IL-17A (#560283). The data were analyzed using Flow Cytometric Analysis Program (FCAP) Array software (BD). Serum IL-22 was measured using LEGEND MAX™ Mouse IL-22 ELISA Kit (BioLegend, #436307) and analyzed using a SpectraMax M2 microplate reader using SoftMax Pro software (Molecular Devices).

RNA preparation and qRT-PCR

ILC2s were sorted into RLT Plus lysis buffer (Qiagen) and stored at – 80 °C until processing using RNeasy Micro Plus kit (Qiagen) per manufacturer's protocol. For quantitative reverse transcriptase PCR analyses, RNA was reverse transcribed using SuperScript VILO cDNA synthesis kit (ThermoFisher) per the manufacturer's instructions. The cDNA was used to test the gene expression of selected genes using Power SYBR Green PCR master mix (ThermoFisher) in a StepOnePlus cycler (Applied Biosystems). The following primers sets from PrimerBank were used: *Il13*: Il13-Forward 5'-CCTGGCTCTTGCTTGCCTT-3' and Il13-Reverse, 5'-GGTC TTGTGTGATGTTGCTCA-3'; *Il22*: Il22-Forward 5'- ATGAGTTTTTCCCTTATGGGGAC-3' and Il22-Reverse 5'- GCTGGAAGTT GGACACCTCAA-3'; *Cdkn2a/p16*: p16-Forward 5'- CGCAGGTTCTTGGTCACTGT-3' and p16-Reverse 5'-TGTTCACGAAAGCCA GAGCG-3'; *Rps17*: Rps17-Forward 5'-CCAAGACCGTGAAGAAGGCTG-3', Rps17-Reverse 5'-GCTGGGGATAATGGCGATCT-3'. Gene expression was normalized to *Rps17* using the ΔCt method.

Chitin Synthase and *Demodex* 18S rRNA gene PCR

For semi-quantitative analyses of *Demodex* burden in skin, three random 2 mm punch biopsies of back caudal skin were digested in digest buffer (10 mM Tris pH 8.0, 100 mM NaCl, 10 mM EDTA pH 8.0, 0.5% SDS and 200 μg/ml Proteinase K (Thomas Scientific)) and the genomic DNA was resuspended in 30 μl of TE. The following primers and PCR conditions were used to detect the highly conserved *Demodex* spp. chitin synthase (CHS) gene (GenBank No. AB080667): CHS-Forward 5'-GAAGCGGCGAGTAATGTT CATC-3'; CHS-Reverse 5'-CCTGACTCCATCTTTTACGATGTC-3'; Cycling conditions 95 °C 3', (95 °C 30", 52 °C 30", 72 °C 30") x 30 cycles, 72 °C 7'. Amplification of the murine Keratin 5 gene was used as a loading control using the following primers and PCR conditions: Keratin5-Forward: 5'-TCTGCCATCACCCCATCTGT-3'; Keratin5-Reverse: 5'-CCTCCGCCAGAACTG TAGGA-3', 95 °C 3', (95 °C 30", 60 °C 30", 72 °C 30") x 30 cycles, 72 °C 7'. PCR products were separated by a 2.5% agarose gel with ethidium bromide and visualized by a GelDoc (Bio-Rad Laboratories). Semi-quantitative analyses of band intensity of CHS and Krt5 was perfomed using Quantity One (version 4.6.1) or Image Lab (version 6.1.0) software (Bio-Rad Laboratories) and reported as the ratio of PCR product of CHS over Krt5. *Demodex musculi* was confirmed by first amplifying the 18S rRNA gene from DNA samples purified from the hair scrapes alone of affected mice using the universal 18S primers and PCR conditions: 18S-Forward 5'-TCCAAGGAAGGCAGCAGGCA-3'; 18S-Reverse 5'-CGCGGTAGTTCGTCTTGCGACG-3', 95 °C 3', (95 °C 30", 58 °C 30", 72 °C 30") x 30 cycles, 72 °C 7'. PCR amplicons (532 bp) were purified and subsequently cloned into pCR4-TOPO plasmid by TOPO-TA cloning (Thermo Fisher) for sequencing. Putative *Demodex* spp. sequences from individual mouse (>3) were identical to the *Demodex musculi* 18S rRNA gene (GenBank No. JF834894).

Preparation of eGFP-CBP for immunofluorescence

Enhanced GFP was cloned into pGV358 (gift from Kushol Gupta, Univ. of Pennsylvania), a pETDuet based vector that has an Mxe intein in frame at the C-terminus followed by the non-cleavable hexahistidine tagged chitin-binding domain from *Bacillus circulans* WL-12 Chitinase A1 (eGFP-CBP). Construct expressing eGFP-CBP (gift from Sy Redding, Univ. of California, San Francisco) was transformed into BL21(DE3) cells and expressed overnight in 50 mL LB media at 37 ºC. 10 mL of overnight culture was diluted in 1L LB media and expressed at 37 ºC until OD_{600} = 1-1.2. Culture was induced with 1 mL 1M IPTG, and expression continued overnight at 19 ºC. We added protease inhibitor (Roche #11836170001) at the temperature change to minimize proteolysis of the expressed protein. Cells were centrifuged at 4,000 x g at 4 ºC for 20 mins. The pelleted cells were resuspended in 50 mL of lysis buffer (100 mM Tris pH 8.5, 150 mM NaCl, 30 mg Lysozyme, protease inhibitor, 1 μL universal nuclease (ThermoFisher Scientific #88700)) per 1 L of culture, then lysed using sonication for 6 mins at 50% power. Lysed cells were centrifuged at 10,000 x g at 4 ºC for 15-30 mins. The lysate supernatant was filtered with a 0.22 μm filter. The filtered lysate was bound to a 5 mL HisTrap FF column (Cytiva #17525501), washed with 100 mM Tris pH 8.5, 150 mM NaCl, 50 mM imidazole pH 7.0, and eluted with a gradient into 100 mM Tris pH 8.5, 150 mM NaCl, 500 mM imidazole pH 7.0. Fractions were selected based on presence of molecular weight band at 56.8 kDa, corresponding with eGFP-CBP, as assessed via SDS-PAGE. Fractions were pooled and dialysed overnight into 100 mM Tris pH 8.5, 150 mM NaCl, 5% glycerol w/v. The protein solution was concentrated and separated via size-exclusion chromatography on a HiLoad 16/600 Superdex 75 pg (Cytiva #28989333). Fractions were selected based on purity as assessed via SDS-PAGE.

Fixed tissue preparation and immunofluorescence staining

For immunohistochemistry, 3-4 mm wide cephalad-caudal strips of back skin were cut and fixed in 2% paraformaldehyde for 2-6 hrs at room temperature, followed by 2 washes in D-PBS, and incubation in 30% (w/v) sucrose in D-PBS at 4 °C overnight. Portions of the tissue sections were submitted for routine paraffin embedding and hematoxylin and eosin staining using UCSF Histology and Biomarker Core. For frozen sections, tissues were embedded in Optimal Cutting Temperature Compound (Tissue-Tek) and stored at –80 °C until further processing. Tissue sections (8-12 μm) were cut on a Cryostat (Leica). Immunohistochemistry was performed in Tris/NaCl blocking buffer (0.1 M Tris-HCl, 0.15 M NaCl, 5 μg/ml blocking reagent (Perkin Elmer), pH 7.5) as follows at RT: 1 hour in 5% goat serum, 1-2 hours in primary antibody, 60 min secondary antibody (Goat anti-Rabbit AF555, 1:1000), 5 min of a 1:1000 dilution of DAPI (Stock 5 mg/ml in PBS), Roche) and mounted in Mounting Media (Vector Labs). The following primary antibodies were used in this study: Living colors DsRed Polyclonal antibody (Rabbit, 1:300, Takara Bio #632496); FITC Anti-mouse Ki67 (1:100, Invitrogen #11-5698-82), and FITC Mouse Anti-E-Cadherin (1:400, BD Biosciences #612131). For detection of chitin in skin tissue sections, 4-5 μm thick paraffin-embedded sections were baked at 60 °C for 30 min, treated with xylenes, and washed with 100% ethanol. The sections were incubated with an eGFP-CBP fusion protein (5 μg/ml) and DAPI (5 μg/ml) in PBS at RT for 60 min, washed 3 times with PBS and mounted using ProLong Gold antifade (Thermo Fisher, P36930). For quantification of HF infested by *Demodex*, two 1.5 to 2 cm strips of back skin from H&E stained sections were evaluated for infestation of hair follicles with a minimum of 70 HF inspected per mouse. Data presented as percentage of HF with at least one mite within the follicle or associated sebaceous gland over total HF visualized. Images were acquired using a Zeiss immunofluorescence AxioImager M2 upright microscope with a Plan Apochromat 20X/0.8NA air objective running AxioVision software (Zeiss) or an inverted Nikon A1R scanning confocal microscope with a Plan Apo λ 20X/0.75NA air objective running NIS Elements software (Nikon).

RNAscope of human tissue samples

Eight cases of normal nose skin were identified by searching the Yale Dermatopathology tissue archive (see Table S4). These cases consisted of the tips of elliptical tissue excisions removing non-melanoma skin cancer. Areas that were well away from

scar were selected for analysis. Eight cases of rhinophyma excision were similarly identified by searching the Yale Dermatopathology archive. RNA in situ hybridization was performed using a chromogenic RNAscope (Bio-techne) assay according to the manufacturer's instructions and as previously described (Wang et al., 2021). The probes were purchased directly from the manufacturer: *IL4* (315191), *IL5* (319391), *IL13* (586241), *IL22* (560811), and *IFNG* (310501). CD3ε IHC was performed using an anti-CD3ε antibody (D7A6E) acquired from Cell Signaling Technology (Danvers, MA). Double staining for CD3ε (IHC) and *IL13* mRNA ISH were performed as previously described (Wang et al., 2021). Briefly, after detection of *IL13* with the RNAscope kit, antigen retrieval was performed with citrate buffer (pH 6.0) (00500, Thermo Fisher Scientific, Waltham, MA). Peroxidase activity was quenched using 3% hydrogen peroxide (JT-2186-01, JT Baker, Phillipsburg, NJ). CD3ε was then hybridized and detected using the Imm-PRESS horseradish peroxidase reagent and diaminobenzidine substrate (Vector Laboratories, Burlingame, CA).

The density of inflammation around the isthmus and infundibular portion of each follicular unit was graded using H&E stained slides and the following scale:

Histologic description	Semi-quantitative score	Log_2 transformation	Score used for statistical analysis
Negligible inflammation	0	-	0
Mild inflammation	1	1^2	1
Modest inflammation	2	2^2	4
Marked inflammation	3	3^2	8
Dense inflammation	4	4^2	16
Very dense inflammation (pseudolymphomatous)	5	5^2	32

The amount of positive staining for each RNAscope probe was quantified on a cell-by-cell basis using the manufacturer's recommendations, with slight modifications. Only inflammatory cells surrounding or within each follicle were scored (there was negligible staining outside these areas). The scoring rubric is summarized below:

ACD score	Scoring criteria
0	No staining*
1	1-2 dots per cell*
2	2-5 dots per cell and no dot clusters
3	5-10 dots per cell and/or <10% of dots are in clusters
4	>10 dots/cell and/or 10% of dots are in clusters

*This intensity of staining is considered background staining and was not included in the quantification.

The slides were scored in a blinded fashion by a board-certified dermatopathologist (W.D.). For CD3ε / *IL13* doublestains the number of CD3ε positive and CD3ε negative cells was manually quantitated. The values were entered into GraphPad Prism. These studies were approved by the Yale IRB (ID 1501015235).

Single cell RNA-seq

C57BL/6J female mice were obtained from Jackson Laboratory at 3 weeks of age and divided into the following groups 1 weeks later: WT control (n = 3), and WT co-housed with *Demodex*-infested *Il4ra*$^{-/-}$ mice for 1 month (n = 3). In a second experiment, WT (uninfected, n = 3) or *Demodex*-infected *Il4ra*$^{-/-}$ (n = 3) and *Il4*$^{-/-}$*Il13*$^{-/-}$ (n = 3) were used for analyses. Single cell suspensions from full thickness skin were stained with antibody to CD45 (to isolate the CD45$^+$ fraction) and integrin alpha 6 to generate a 50:50 representation of CD45$^-$alpha6$^+$ and CD45$^-$alpha6$^-$ cells in the CD45$^-$ fraction. Cell suspensions were stained with DAPI and live cells (DAPI$^-$) were isolated by FACS using a MoFlo XDP (Beckman Coulter). The concentration of sorted cells was determined using CountBright beads on an LSRFortessa. Single-cell libraries from 25,000 cells per sample were prepared with the Chromium Single Cell 3' GEM, Library & Gel Bead Kit v3.1 (10 x Genomics PN-1000121) following the manufacturer's protocol. The libraries were sequenced on the NovaSeq 6000 at the UCSF Institute for Human Genetics with the following number of cycles for each read: Read 1, 28 cycles; i7 Index, 8 cycles; i5 Index, 0 cycles; Read 2, 91 cycles.

Data were analyzed in Seurat V3 or V4 in R using SCTransform aggregation, 0.6 resolution, with the following quality parameters: min.cells =5, nFeature_RNA > 500; nFeature_RNA< 5000; nCount_RNA < 25000; percent mitochondrial reads < 15; percent hemoglobin reads 0.001. Percentage mitochondrial and ribosomal content were regressed out of clustering and aggregation. After initial clustering, cell identities in the CD45$^-$ fraction (epithelia, fibroblasts, other stromal cells) were assigned using public data sets (Joost et al., 2020). CD45$^+$ immune clusters were identified by canonical markers and subclustered. Doublets were removed and the

populations were clustered again before differential expression (DEG) analysis for cluster-defining genes and differential expression between treatment conditions. Data generated from different experiments (WT control vs. WT Demodex+; WT uninfected vs. *Il4ra*$^{-/-}$ Demodex+ vs. *Il4*$^{-/-}$*Il13*$^{-/-}$ Demodex+) were integrated using the R package Harmony prior to clustering cell types. Batch correction was performed by creating a binary batch variable between the two datasets.

For DEG analysis between clusters, genes were detected if they are expressed in at least 10% of cells in a cluster with a log-fold change of at least 0.25. For DEG analysis between comparison groups within each cluster, genes were detected if expressed in at least 10% of cells in the group with a log-fold change of at least 0.25. For DEG analysis comparisons for all cells in aggregate, genes were detected if expressed in at least 10% of cells and with a log-fold change of at least 0.10. Additionally, for within-cluster DEG analysis, analysis was only done for clusters with >30 cells in each comparison group. Gene ontology (GO) term pathway analyses was performed using GOrilla (http://cbl-gorilla.cs.technion.ac.il) by inputting 'pseudo'-bulk DEGs, from all CD45 negative cells, that were upregulated with a log-fold change of at least 0.2 in *Demodex*-infected WT, *Il4ra*$^{-/-}$ or *Il4*$^{-/-}$*Il13*$^{-/-}$ mice vs. the experimental WT control. Additional data visualization was performed using the Nebulosa package in Seurat (https://github.com/powellgenomicslab/Nebulosa).

In Figures S7H–S7J epidermal stem cells were identified among subclustered epithelial cells by differential expression of *Lgr5*, *Cdh3*, *Gli1* and/or *Mki67*. DEGs among all stem and dividing cells between conditions were identified by expression in at least 10% of cells with a $\log_2$ fold change of at least 0.10 between condition. GO Term enrichment was performed using EnrichGO in the ClusterProfiler package in R (Yu et al., 2012).

Transepidermal water loss measurements

Transepidermal water loss (TEWL) measurements were performed as described (Mathur et al., 2019). Briefly, mice back were shaved and rested for 18-24 h. Mice were sedated and TEWL was measured on four quadrants of back skin using a Tewameter (TM300, Khazaka Electronic).

Lucifer yellow assay to assess barrier function

Back skin from WT or *Il4ra*$^{-/-}$ mice was shaved and depilated. Two days after depilation, skin was harvested, washed twice with PBS and placed on a 7 mm Franz-Cell chamber (PermeGear Inc). The epidermal surface was incubated with Lucifer yellow (L453, ThermoFisher, 1 mg/ml) in PBS for 18 h at 37 °C. Samples were fixed for 1 h in 4 % PFA, washed twice with PBS, embedded in OCT and processed for immunofluorescence imaging.

16S rRNA gene sequence analysis

Sample collection

Mice facial and back skin were swabbed at the end of the experiment using a sterile foam tipped applicator (Puritan) that was moistened with yeast cell lysis buffer (Lucigen) and collected into sterile 2 ml tubes (Eppendorf). All samples were immediately snap frozen in dry ice and stored at –80 °C until DNA extraction.

DNA extraction and V1V3 Library Prep

DNA was extracted from samples using the DNEasy PowerSoil Pro Kit (Qiagen) according to the manufacturer's protocol. Barcoded PCR primers annealing to the V1-V3 region of the 16S rRNA gene (Fwd, 5'-AGAGTTTGATCCTGGCTCAG-3'; Rev, 5-ATTACCGCGGCTGCTGG-3') were used for library generation. PCR reactions were carried out in quadruplicate using Q5 High-Fidelity DNA Polymerase (NEB, Ipswich, MA). Each PCR reaction contains 0.5 μM of each primer, 0.34 U Q5 Pol, 1X Buffer, 0.2 mM dNTPs, and 5.0 μl DNA in a total volume of 25 μl. Cycling conditions are as follows: 1 cycle of 98 °C for 1 min; 30 cycles of 98 °C for 10 sec, 56 °C for 20 sec, and 72 °C for 20 sec; 1 cycle of 72 °C for 8 min. After amplification, quadruplicate PCR reactions were pooled and then purified using a 1:1 volume of SPRI beads. DNA in each sample was quantified using PicoGreen and pooled in equal molar amounts. The resulting library was sequenced on the Illumina MiSeq using 2x300 bp chemistry. Extraction blanks and DNA free water were subjected to the same amplification and purification procedure to allow for empirical assessment of environmental and reagent contamination.

Bioinformatics processing

Sequence data were processed using QIIME2 (Bolyen et al., 2019). Read pairs were processed to identify amplicon sequence variants with DADA2 (Callahan et al., 2016). Taxonomic assignments were generated by comparison to the Greengenes reference database (McDonald et al., 2012), using the naive Bayes classifier implemented in scikit-bio (Bokulich et al., 2018). A phylogenetic tree was inferred from the sequence data using MAFFT (Katoh and Standley, 2013).

Statistical analysis for microbiome data

Data files from QIIME were analyzed in the R environment for statistical computing, using the QIIMER library, which we developed (http://cran.r-project.org/web/packages/qiimer). Global differences in bacterial community composition were visualized using Principal Coordinates Analysis of weighted and unweighted UniFrac distance (Lozupone and Knight, 2005; Lozupone et al., 2007). Community-level differences between sample groups were assessed using the PERMANOVA test, which allows sample-sample distances to be applied to an ANOVA-like framework (Anderson, 2001). Linear mixed-effects models were used to ascertain differences in alpha diversity and taxonomic abundances.

Statistical analysis

All experiments were performed using randomly assigned mice without investigator blinding. All data points and n values reflect biological (individual mice) replicates. Experiments were pooled whenever possible, and all data were analyzed using Prism 7 (GraphPad Software) by comparison of means using unpaired two-tailed Student's *t* tests or one-way ANOVA for multiple comparison as indicated in the figure legends. Data in all figures displayed as mean ± s.e.m. unless otherwise indicated.